A muon veto for the measurement of the downgoing neutrino flux with KM3NeT/ORCA

Masterarbeit aus der Physik

vorgelegt von

Marco Volkert

03.02.2017

Erlangen Centre for Astroparticle Physics
Physikalisches Institut
Friedrich-Alexander-Universität Erlangen-Nürnberg

1. Gutachter: Prof. Dr. Gisela Anton
2. Gutachter: Prof. Dr. Uli Katz

Contents

Abstract

By measuring the energy- and zenith-dependent oscillation probabilities of atmospheric neutrinos passing through the Earth, it is possible to determine the hitherto unknown neutrino mass hierarchy. With this aim, the underwater Cherenkov detector ORCA is being built by the KM3NeT Collaboration in the Mediterranean deep sea. The atmospheric muon flux entering the detector from the direction of the water surface is the main background for the detection of neutrinos.

On the one hand, incorrectly reconstructed tracks of atmospheric muons distort the measurement of the upgoing atmospheric neutrino flux passing through Earth. On the other hand, this background crucially complicates the measurement of the downgoing atmospheric neutrino flux from above, which could be used for reducing the systematic uncertainties, as it is not modified by neutrino flavour oscillations.

In this thesis a veto strategy for atmospheric muons is developed in order to allow the determination of the downgoing atmospheric neutrino flux. The presented veto algorithm achieves a remaining contamination by atmospheric muons of less than $15\,\%$ by only applying fast classification methods on the pattern of the first hits. By applying standard event reconstruction methods in addition, the contamination can further be decreased to about $1\,\%$. The effective mass for neutrinos after the muon veto cut is roughly about $1.75\,\mathrm{Mton}$ for the neutrino energy regime above $10\,\mathrm{GeV}$, which corresponds to about nearly $50\,\%$ of the effective volume for upgoing neutrinos of a $6\,\mathrm{m}$ vertical spaced detector.

Furthermore an investigation is presented on the achievable precision with which the atmospheric neutrino flux parameters can be determined within one year, assuming the detection of downgoing neutrinos with the obtained effective mass. The reachable uncertainty on the neutrino flux normalization depends on how well the energy scale (detector intrinsic linear energy scaling factor) can be determined by using other calibration methods, as both are fully correlated. The neutrino flux zenith slope cannot be determined much better than it is known so far.

Chapter 1

Introduction

Neutrinos are very interesting fermions of the Standard Model of Particle Physics (SM). They have an extremely low cross-section of about 10^{-42}m^2 at $1\,\text{GeV}$ and thus can traverse nearly every medium without a reaction. Solar neutrino studies gave the insight that neutrinos change their flavour [1]. This behaviour is called neutrino oscillation and its existence implies that neutrino have mass, unlike predicted by the SM. Thus neutrinos give a hint to physics beyond the SM. Besides studies on solar neutrinos, experiments were performed with atmospheric, reactor and accelerator neutrinos. Various experiments of those kinds measured the parameters of the neutrino oscillation.

One of the still unknown parameters is the sign of the largest mass difference, called neutrino mass hierarchy (NMH). This sign is determinable via oscillations in matter. The KM3NeT-Collaboration builds the Cherenkov detector ORCA in the Mediterranean deep sea to use atmospheric neutrino traversing the Earth for probing the NMH.

One crucial systematic for the neutrino mass hierarchy measurement is the uncertainty on the neutrino flux normalization. Therefore, an independent calibration measurement of downgoing neutrinos is intended. However, the many orders of magnitude greater rate of atmospheric muons complicates this calibration measurement. The idea how to deal with this is to use some kind of fiducializing as it is used in similar detectors.

This thesis is organised in the following way: at first, chapter 2 gives an introduction to the origin of neutrinos and their physics, as well as to the detector structure, simulation and performance. Then chapter 3 deals with the implementation of the muon veto. Accordingly it addresses following questions: why is a veto needed (Sec. 3.1), what steps have been taken to implement it (Sec. 3.2 and Sec. 3.3) and how well does it behave (Sec. 3.4). Finally chapter 4 presents the theoretical uncertainties on neutrino flux parameters (Sec. 4.1) and how well those could be determined by using the muon veto for a downgoing flux measurement (Sec. 4.3).

Chapter 2

Scientific background

2.1 Atmospheric fluxes
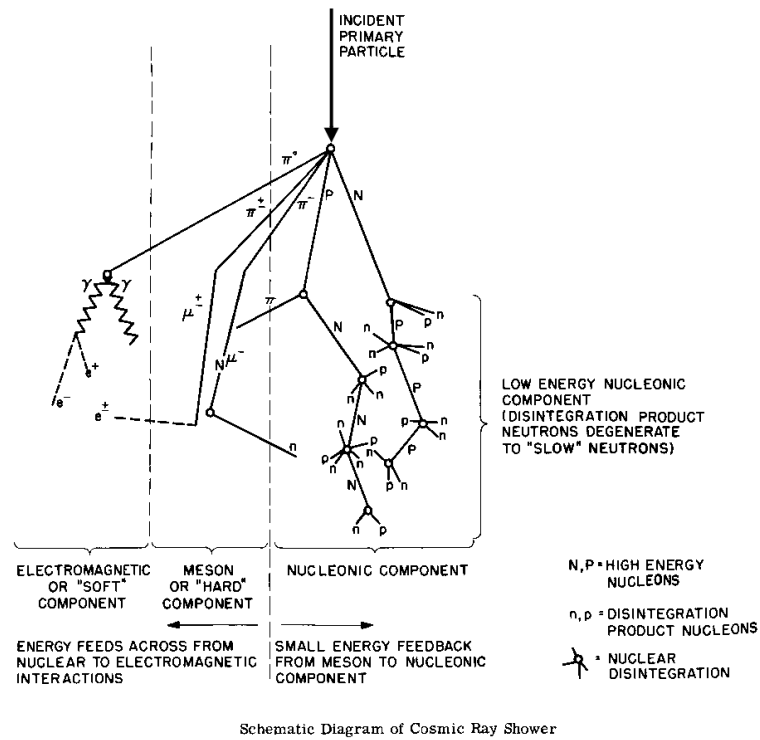
Figure 2.1: Atmospheric particle cascade caused by cosmic rays. Taken from [2].

There is a diffuse flux of charged cosmic ray particles, mainly protons and some heavier nucleons, hitting the Earth's atmosphere. This flux mainly follows a power-law in energy $N(E) \propto E^{-\gamma}$, with $\gamma \sim 2.7$ [3]. Secondary 'atmospheric' cosmic rays are produced by collision of primary comic rays with atmospheric particles. These are often called cosmic ray showers, as the primary particles are energetic enough to produce a whole cascade of particles. Produced protons and neutrons will

3

continue to cause particle showers because of their high energy and large cross-section, whereas pions immediately decay into e.g. muons and neutrinos. The low cross-section of muons causes lower energy loss compared to nucleons. Furthermore muons are highly relativistic due to their high energy and therefore can reach sea level despite their short lifetime of $2,2 \cdot 10^{-6}$ s [3]. Thus, muons are the dominating part of the secondary cosmic rays reaching the sea level. Muons, which decay on their way to sea level, produce neutrinos. The main decay chains are given by Eq. 2.1 and the formula's charge conjugation.

$$\pi^- \to \mu^- + \overline{\nu}_\mu \text{ and } \mu^- \to e^- + \nu_\mu + \overline{\nu}_e \tag{2.1}$$

If all muons decay the expected ratios are:

$$\frac{\nu_\mu + \overline{\nu}_\mu}{\nu_e + \overline{\nu}_e} \sim 2 \quad , \quad \frac{\nu_\mu}{\overline{\nu}_\mu} \sim 1 \quad \text{and} \quad \frac{\nu_e}{\overline{\nu}_e} \sim \frac{\mu^+}{\mu^-}. \tag{2.2}$$

The more energetic the muons are, the less muons decay before reaching ground and therefore the ratio of muon to electron neutrinos changes. In the absence of neutrino oscillations the neutrino flux is in good approximation up/down symmetric, although it is not exact for $1\,\text{GeV}$ or less due to geomagnetic field effects. The muon flux was measured by various experiments at different energies and altitudes [4]. MUPAGE provides a parameterised muon event generation for muon background investigations in Cherenkov neutrino telescopes [5]. The parametrization is based on full simulations and cosmic ray data. Single muons as well as muon bundles are included.

2.2 Neutrino oscillation

Oscillation in vacuum

The phenomenon that neutrinos change their flavour during propagation is called neutrino oscillation. This happens because the neutrino flavour eigenstates are a mix of the neutrino mass eigenstates (Eq. 2.3). In 2015 T. Kajita and A. B. McDonald were awarded the Nobel Prize for this discovery. All following formulas are given in natural units and are mainly adopted from [6].

$$\begin{pmatrix} \nu_e \\ \nu_\mu \\ \nu_\tau \end{pmatrix} = U_{\text{PNMS}} \cdot \begin{pmatrix} \nu_1 \\ \nu_2 \\ \nu_3 \end{pmatrix}, \quad U_{\text{PNMS}} = \begin{bmatrix} 1 & 0 & 0 \\ 0 & c_{23} & s_{23} \\ 0 & -s_{23} & c_{23} \end{bmatrix} \cdot \begin{bmatrix} c_{13} & 0 & s_{13}e^{-i\delta} \\ 0 & 1 & 0 \\ -s_{13}e^{i\delta} & 0 & c_{13} \end{bmatrix} \cdot \begin{bmatrix} c_{12} & s_{12} & 0 \\ -s_{12} & c_{12} & 0 \\ 0 & 0 & 1 \end{bmatrix}, \tag{2.3}$$

with mixing angles: $s_{ij} = \sin\theta_{ij}$ and $c_{ij} = \cos\theta_{ij}$ and with the CP-violating phase: δ;
possible majorana phases were neglected.

The time evolution of a propagating neutrino is given by a plane wave:

$$|\nu_k(t)\rangle = \exp(-i(E_k t - \vec{p}_k \cdot \vec{x}))|\nu_k(0)\rangle, \tag{2.4}$$

where E_k is the energy and $\vec{p}_k$ the momentum of the neutrino.

In the ultra relativistic limit ($E_k >> m_k$) the following approximation holds:

$$|\vec{p}_k| = \sqrt{E_k^2 - m_k^2} \approx (E_k - \frac{m_k^2}{2E_k}) \rightarrow E_k t - \vec{p}_k \cdot \vec{x} \approx \frac{m_k^2}{2E_k} L. \tag{2.5}$$

The probability for detecting a neutrino produced in flavour state ν_α with flavour ν_β after propagating over a distance L is given by the square of the transition amplitude:

$$P_{\nu_\alpha \rightarrow \nu_\beta}(L) = |\langle \nu_\beta | \nu_\alpha(t) \rangle|^2 = \sum_{k.j} U_{\alpha k}^* U_{\beta k} U_{\alpha j} U_{\beta j}^* \exp\left(-i\frac{\Delta m_{kj}^2 L}{2E_k}\right), \tag{2.6}$$

with the mass-squared difference $\Delta m_{kj}^2 = m_k^2 - m_j^2$.

For simplicity of an example only the two flavour case (ν_e and ν_μ) is considered. If Φ_{ν_e} and Φ_{ν_μ} are the incoming fluxes, the detected fluxes will be:

$$\Phi'_{\nu_e} = P(\nu_e \rightarrow \nu_e)\Phi_{\nu_e} + P(\nu_\mu \rightarrow \nu_e)\Phi_{\nu_\mu} \tag{2.7}$$
$$\Phi'_{\nu_\mu} = P(\nu_e \rightarrow \nu_\mu)\Phi_{\nu_e} + P(\nu_\mu \rightarrow \nu_\mu)\Phi_{\nu_\mu}.$$

Oscillation in matter

During propagation through matter the neutrinos are coherently elastically scattered by electrons and nucleons (see Fig. 2.2). NC-interactions happen for all flavours, so they just add a flavour independent phase shift. Yet only electron neutrinos can undergo CC-interaction, because electrons are the only charged leptons in matter. This leads to an alteration of the propagation of electron neutrinos described by the effective potential $V_{\text{CC}} = \pm\sqrt{2}G_F N_e$, where G_F is the Fermi coupling constant and N_e the electron number density. The '+' is valid for neutrinos and the '−' is valid for antineutrinos.
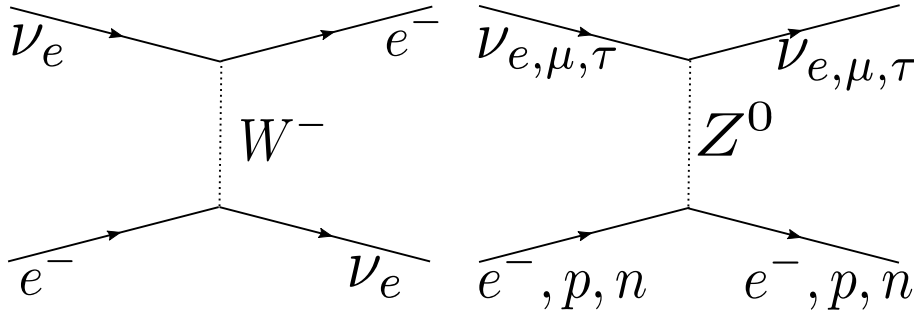

Figure 2.2: Neutrino coherent elastic scattering: charged current (CC) interaction conveyed by $W^\pm$(left) and neutral current(NC) interaction conveyed by Z^0 (right). Only electron neutrinos can undergo CC-interaction.

The change in propagation causes a change in the mass eigenstates and a change of the mixing angles (the new mixing angle has the suffix m for 'matter'):

$$\sin^2 2\theta_m = \sin^2 2\theta \frac{1}{\left(A - \cos 2\theta\right)^2 + \sin^2 2\theta},$$

(2.8)

with $A = \frac{2V_{\mathrm{CC}}E_\nu}{\Delta m_{kj}^2}$. This is commonly called the MSW-effect [1]. (However, the term originally describes the adiabatic oscillation probability change in the sun, which solved the solar neutrino problem.) $A \approx \cos 2\theta$ implicates a resonance where θ_m becomes maximal ($45°$). If $\Delta m_{kj} > 0$, the resonance occurs for neutrinos, otherwise for anti neutrinos. The energy at which the resonance happens is then given by:

$$E_\nu^{res} = \frac{\Delta m_{kj}^2 \cdot \cos 2\theta_{kj}}{2\sqrt{2}G_F N_e}.$$

(2.9)

The resonance involving Δm_{21} was detected via solar neutrino observation by the SNO experiment [8]. The Δm_{21} was determined to be positive, whereas resonance involving Δm_{31} happens in the Earth. By inserting the typical density of rock: $\rho = 3\,\mathrm{g/cm}^3 \rightarrow E_{Res} = 10\,\mathrm{GeV}$ and the Earth's core $\rho = 13\,\mathrm{g/cm}^3 \rightarrow E_{Res} = 2\,\mathrm{GeV}$, it can be seen that the resonance energy is in the range of a few GeV. Even at energies which are not at the resonance value the oscillation probability can significantly be enhanced due to abrupt Earth density transitions, particularly between Earth's mantel and Earth's core. This is called 'parametric enhancement' [9], but this is not further relevant in the scope of this thesis.

2.3 Neutrino mass hierarchy

Vacuum oscillation of neutrinos is only dependent on the mixing angles, a possible CP-violating phase and the squared mass difference of the mass eigenstates. As seen in the previous section, the sign of the mass difference can be deduced using the MSW resonance. The sign of Δm_{12} is known from solar neutrino studies, whereas the sign of $\Delta m_{13}/\Delta m_{23}$ is hitherto unknown. The question about this sign is called **neutrino mass hierarchy** (NMH) which can either be normal (positive sign) or inverted (negative sign) (see Fig. 2.3). Recently (2012,[11]) the last unknown mixing angle θ_{13} was measured to be relatively large ($\sim 9°$). This drove the determination of the NMH within reach [12]. The standard strategy
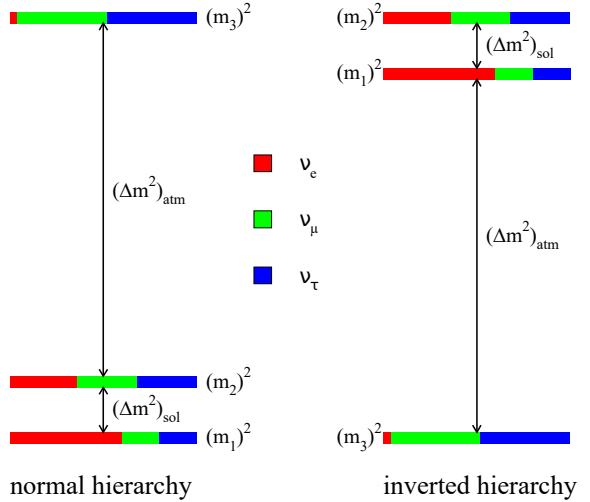

Figure 2.3: Neutrino mass hierarchy - left: normal, right: inverted - Taken from [10].

for NMH determination is to probe $\nu_e \Leftrightarrow \nu_\mu$ oscillation in presence of matter effects. The oscillation enhancement of matter effects is maximal at resonant energy which is $E_{\mathrm{res}} \sim$ few GeV for the Earth matter density. Therefore there are good prospects for NHM determination with

---

[1] Michejew-Smirnow-Wolfenstein [7]

atmospheric neutrinos traversing the Earth. Energy(E)-zenith(θ_z)-oscillograms show a distinctive pattern for NH and IH (see Fig. 2.4 and Fig. 2.5). The main challenges are that the NH/IH difference is intrinsically small and that oscillograms are blurred by limited E and θ_z accuracy.
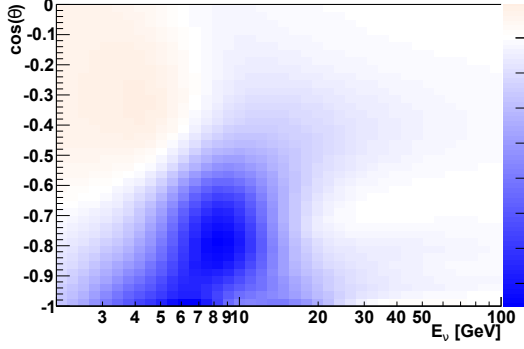

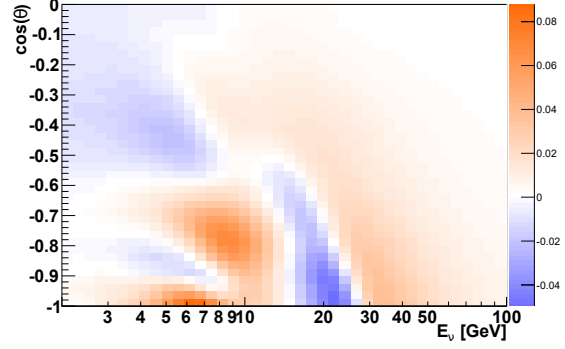Figure 2.4: NH-IH-asymmetry for ν_e - Taken from [13].

Figure 2.5: NH-IH-asymmetry for ν_μ - Taken from [13].

2.4 Cherenkov detectors

When a charged particle traverses a medium with a velocity greater than the speed of light in the medium, Cherenkov light is emitted in a cone with an opening angle of $\theta_C = \arccos \frac{1}{n\beta}$, with the refractive index n and $\beta = v/c$ (see Fig. 2.6). For $n_{\text{water}} \approx 1.3$ and $\beta \approx 1$ the angle is about $43°$. Cherenkov detectors detect this light using photomultipliers (PMTs) in a transparent medium like water or ice. PMTs make use of the photoelectric effect to convert photons into a electron cascade. Their efficiency, called quantum efficiency, is about $\sim 25\%$. From the amplified electron cascade the time and charge information is deduced and called a *hit*. These PMTs are arranged within a digital optical module (DOM) and an array of several DOMs builds up the detector. Neutrinos can be detected by Cherenkov

Figure 2.6: Cherenkov light

detectors through their secondary particles produced during an interaction with the medium. At relevant energies (above $3\,\text{GeV}$) deep inelastic scattering (DIS) dominates, therefore, the neutrino scattering of a nucleon causes a hadronic cascade and an outgoing lepton.

The main discrimination is made between charged current (CC) and neutral current events (NC) (see Tab. 2.1). A CC event can be written as $\overset{(-)}{\nu}_l + N \rightarrow l^\pm + X$, where l is a lepton, N a nucleon and X a hadronic cascade. Electrons (e) travel a short path length ($\sim 33\,\text{cm}$) till
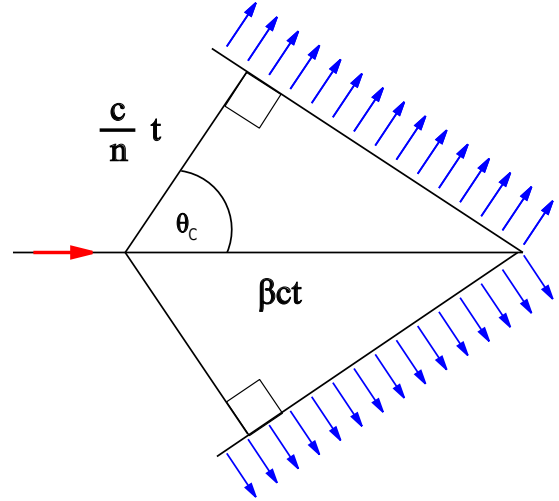
interaction produces an electromagnetic shower. Muons (μ) are minimal ionising particles (mip) at energies above $1\,\text{GeV}$ and therefore have a high mean free path, i.e. are track-like. Tauons (τ) decay after short path such that they appear either shower-like or track-like, depending on their decay channel. But tau-neutrinos can be ignored in the scope of this thesis. In an NC event instead of a charged lepton a neutrino is produced escaping without detection. Only the hadronic cascade is visible.
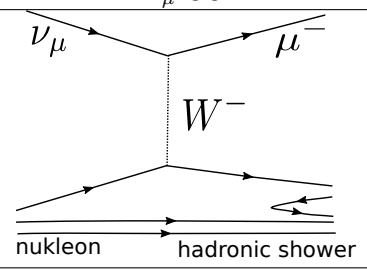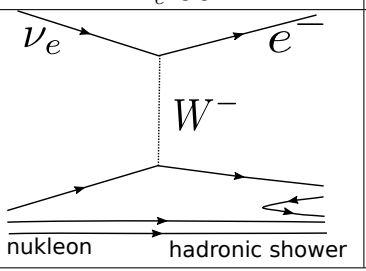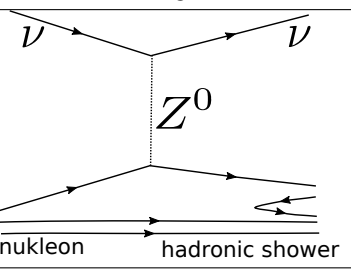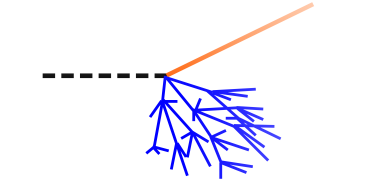

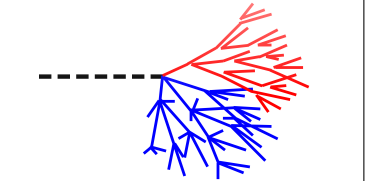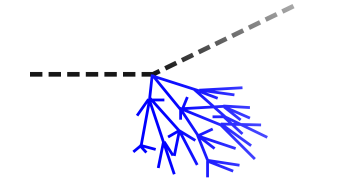| ν_μ CC	ν_e CC	NC
track-like	shower-like or point-like	
hadronic shower and μ-track	hadronic and EM shower	hadronic shower

Table 2.1: Neutrino interactions

2.5 ORCA: Oscillation Research with Cosmics in the Abyss

KM3NeT is the next generation underwater neutrino telescope in the Mediterranean Sea with two detectors: **ARCA** and **ORCA** - Astroparticle/Oscillation Research with Cosmics in the Abyss. Both of them use the same technology and detector design: one building block consists of 115 instrumented lines, called 'strings', which are anchored to the seabed. Each string carries 18 digital optical modules (DOMs). Every DOM consists of 31 PMTs arranged in five rings with same zenith angle and an additional PMT pointing downward (Fig. 2.7).

ARCA's main objective is the high-energy neutrino astronomy and is intended to get a square kilometre large volume like IceCube, whereas ORCA is primarily built for the NMH determination at lower energy. Thus ORCA is more densely built than ARCA: optimal parameters (taking deployment constraints into account) were deter-

Figure 2.7: Digital optical module (DOM) - Taken from [13].

mined to be an average $20\,\text{m}$ inter-string spacing and $9\,\text{m}$ vertical spacing between the DOMs (Fig. 2.8, Fig. 2.9).
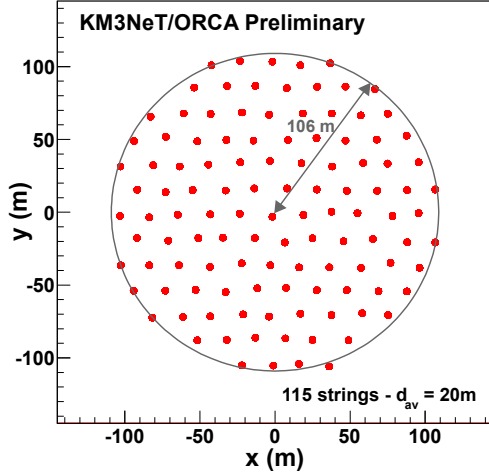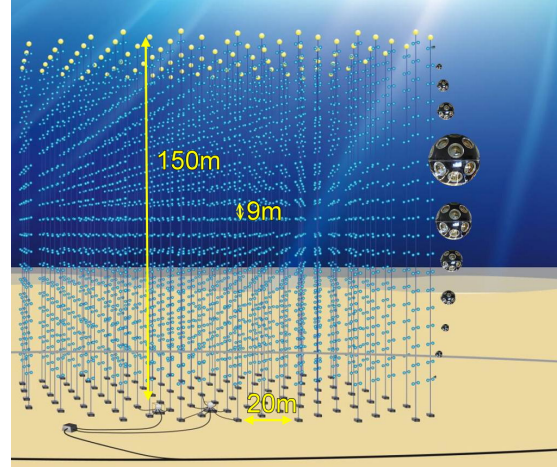
Figure 2.8: ORCA Footprint. Taken from [13].

Figure 2.9: ORCA Building Block. Taken from [13].

2.6 Simulation of ORCA

A full Monte Carlo detector simulation of particle interactions, light generation, light propagation and detector response has been performed in the Letter of Intent [13]. The simulation is conducted within a cylindrical volume surrounding the instrumented volume, called 'can'. This 'can' exceeds the instrumented volume by about 40 m. The common neutrino event generator GENIE [15] is used for generation of (anti-)neutrino induced interactions in sea water in the energy range from 1 to 100 GeV. Those neutrino events have (Bartol [16]) flux weightings, because the simulation is made with a less steep spectrum to have more statistics at high energies. Muon background is simulated using MUPAGE [5]. Particle propagation is then simulated by a software package based on GEANT4: Cherenkov light generated by primary and secondary particles causes hits, thereby the light absorption and scattering in the medium as well as the detector characteristics are taken into account. Additionally random background noise is simulated. Hit selection and analysis scripts, which have been used or developed in this thesis, are written in python within the software package Seatray [17].

2.7 Performance of ORCA

This section presents the main performance parameters of ORCA, namely the detection efficiency and sensitivity to the main measurement that were determined by using the previously described simulation.

The neutrino detection efficiency ν_{eff} can be defined as the interaction rate of detected neutrinos R^{ν}_{det} divided by the interaction rate of generated neutrinos R^{ν}_{gen}, which were generated within a generation volume V_{gen}. V_{gen} is chosen in a way that the secondary leptons would pass the detector.

The effective volume V_{eff} is then calculated in the following way:

$$V_{\text{eff}} = \nu_{\text{eff}} \cdot V_{\text{gen}} = \frac{R^{\nu}_{\text{det}}}{R^{\nu}_{\text{gen}}} \cdot V_{\text{gen}}. \tag{2.10}$$

The effective volume can be converted into an effective mass M_{eff} by using the water density $\rho = 1.025\,\text{g/cm}^3$: $M_{eff} = \rho V_{\text{eff}}$. The effective mass is a measure for the efficiency of a detector that can be compared between detectors. It expresses how much mass a $100\,\%$ efficient detector would encompass. Fig. 2.10 shows the effective mass of well reconstructed events as a function of energy for different detector sizes. Full simulation of muon and neutrino events was only made for a detector with $6\,\text{m}$ vertical spacing [13]. Detector response for larger spacing were calculated in the following way: a mean larger spacing is achieved by ignoring some DOMs and then account for fewer DOMs by scaling the result accordingly. As the developed muon veto (see chapter 3) explicitly looks at the position and number of individual DOM hits, this procedure does not work well in this case. Therefore, the muon veto was optimised and evaluated for a $6\,\text{m}$ vertical spacing. To apply it to the detector with $9\,\text{m}$ vertical spacing, some parameters of the veto have to be upscaled.

The sensitivity for mass hierarchy determination is dependent on the oscillation parameters, especially on the true mixing angle θ_{23} (see Fig. 2.11). The highest sensitivity to the NMH is reached in the case of $9\,\text{m}$ vertical spacing. Therefore, this vertical spacing will be chosen for the construction. The NMH can be determined to about $3\,\sigma$ after 3 years.
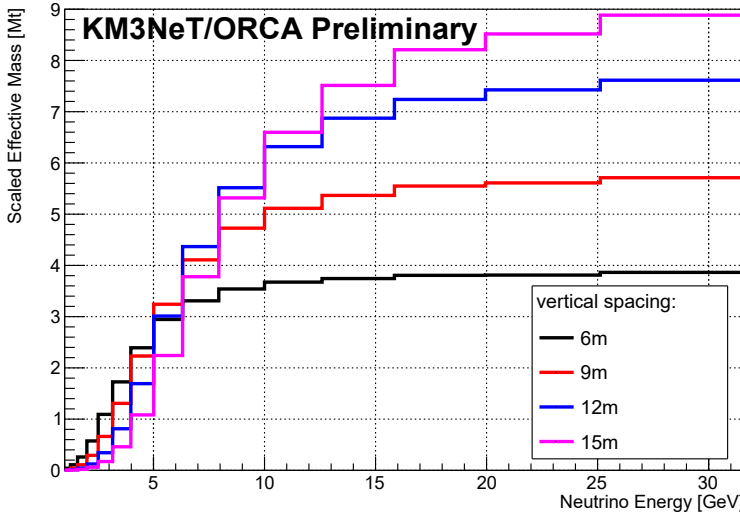

Figure 2.10: Effective mass for ν_μ and $\overline{\nu}_\mu$ as a function of the neutrino energy for well reconstructed events. - Taken from [13].
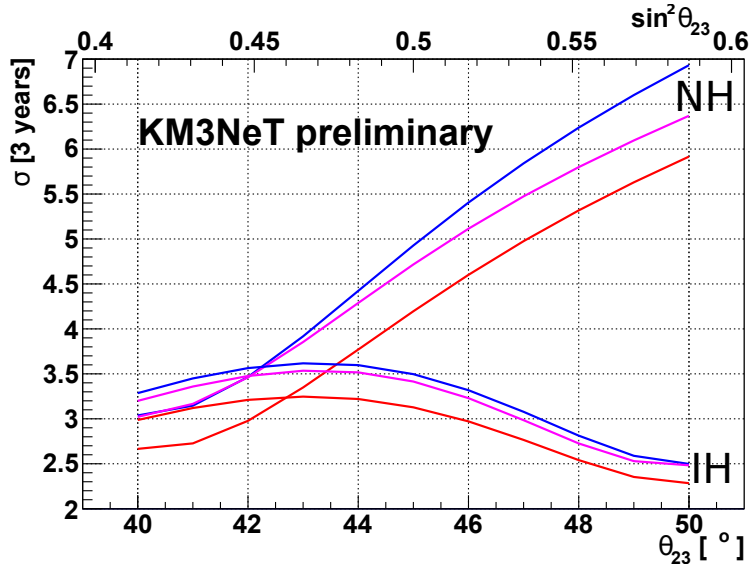
Figure 2.11: NMH Sensitivity for 3 years of data taking as function of the true mixing angle θ_{23} for both hierarchy hypotheses. Different vertical distances between adjacent DOMs are simulated: red 6 m, blue 9 m, magenta 12 m. - Taken from [13].

Chapter 3

Implementation of the Muon Veto

3.1 Aim and approach

3.1.1 Misreconstructed muons

The main measurement of ORCA will be the precise determination of the oscillated neutrino flux traversing the Earth. No other particles, like muons, can traverse the Earth. Therefore, by selecting only events reconstructed as upgoing, the main part of muons is suppressed. Only muons which are falsely reconstructed as upgoing are still a background. This background has already been dealt with in the Letter of Intent [13]: reconstruction (reco) parameters like the *fit quality* and *track starting point* (more precisely described in Sec. 3.3.4) can directly be used as the preselected background is small.
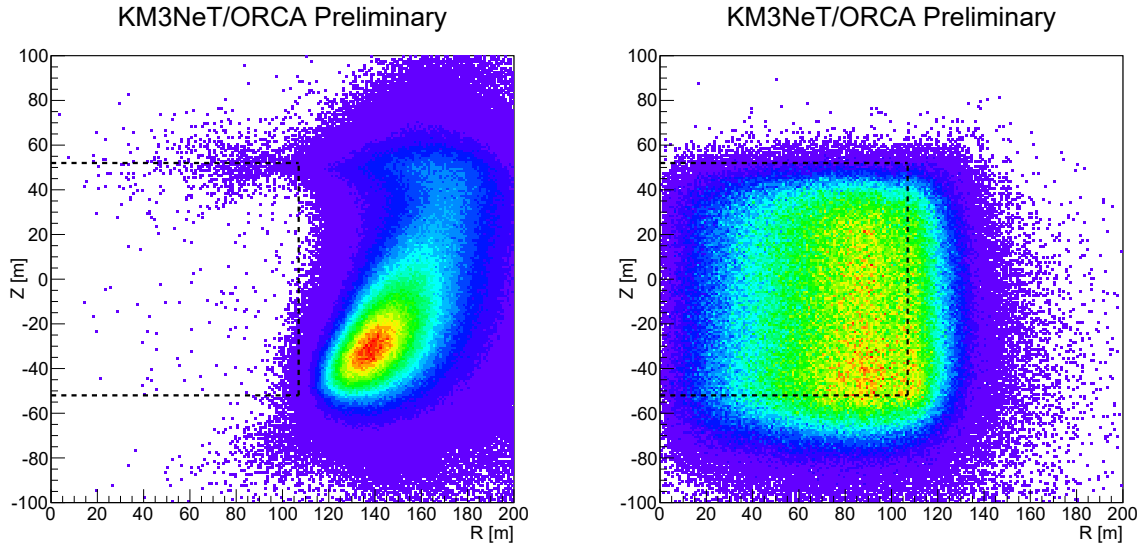

Figure 3.1: Distribution of the reconstructed track starting point for muons (left) and neutrinos (right). Taken from [13].

3.1.2   Atmospheric neutrino flux measurement

One crucial systematic uncertainty for the neutrino mass hierarchy measurement is the overall normalisation of the neutrino flux (see Sec. 4.1). Thus a neutrino flux measurement independent from the matter oscillation resonance, used for the mass hierarchy determination, would be a good way to calibrate the NMH measurement. However, just looking at slightly higher energies, which are not effected by the resonance, would not make the deal, as there is still flavour oscillation. So to be really independent, this calibration measurement has to be conducted with downgoing neutrinos in an energy regime of about $10\,\text{GeV}$ to $60\,\text{GeV}$. However, the main problem for downgoing events is that there is a large background of atmospheric muons to be dealt with:

The trigger rate of downgoing muon neutrino CC interaction-rate is ~ 150 per day ($\sim 5 \cdot 10^4$ per year), whereas the trigger rate of atm. muons is about $\sim 40\,\text{Hz}$ ($\sim 10^9$ per year). Therefore, in order to achieve a contamination lower than $1\,\%$, a muon suppression of more than 10^6 is required. Full event reconstruction is too time-consuming to be run at $\sim 40\,\text{Hz}$ so that a fast algorithm to suppress the main part of muons is needed before reco-methods (Sec. 3.3.4) can be applied.

The idea is to use some kind of fiducializing as it is used in similar detectors (e.q. IceCube [18] and Super-Kamiokande [19]). So the pattern of the first hits of an event should give information about whether the event started outside of the fiducial volume or not. At first there has to be a very clean hit selection to be confident that the hits, from which the information shall be deduced, are not noise hits (see Sec. 3.2). Then various parameters describing the pattern of the first hits can be calculated and cuts can be applied (see Sec. 3.3.1). When the remaining muon rate is at least as low as the neutrino rate, full reconstruction similar to the one used to identify misreconstructed muons (Sec. 3.1.1) can be conducted and cuts on the obtained parameters can be applied (see Sec. 3.3.4).

For a rough estimation of the required computational time, the time per muon event on the 'standard' computer at the computing centre in Lyon [20] is given:

- hit selections: $0.41\,\text{s}$

- rejection criteria without reconstruction: $0.08\,\text{s}$

- full reconstruction: $7.7\,\text{s}$ [2]

3.1.3   Event display

In order to find parameters to distinguish muons and neutrinos from each other, an event display optimised for this task has been developed. As the detector is radial symmetric, mainly the radial projection is important. The radius is scaled quadratically so that areas of the same size correspond to volumes of the same size. On the y-axis the height in floor numbers is plotted. For a better visualisation, the DOM-positions are chosen to be extended over the floor height and their upper edge corresponds to the floor they belong to. The DOM hit colour denotes the time since the first hit (after hit selection) of the event. The Monte Carlo truth muon track is painted in black and the reconstructed track is painted in red. Black crosses label the interaction vertex, red ones the reconstructed vertex (track starting point) and green ones the mean position of first hits (see

---

[2]The duration of the reconstruction scales with the number of hits of an event, whereby the average muon event has quite a lot of hits. Applying reconstruction only on less luminous events would lower the average time.

Sec. 3.3.1). Arrows display the mean direction of PMT hits on a DOM. An example for the event display of a muon event is shown in Fig. 3.2.
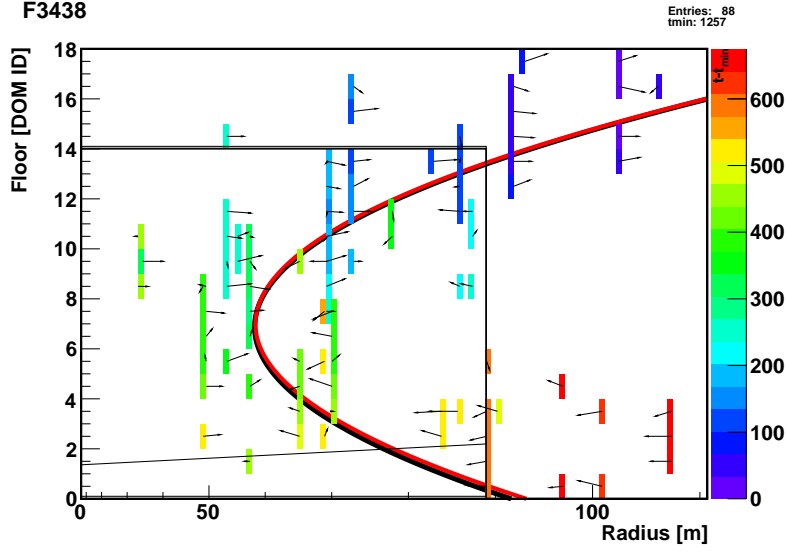

Figure 3.2: Event display of a muon event - black: Monte Carlo truth particle track, red: reconstructed track, green: mean position of first hits, arrows: mean direction of PMT hits on a DOM. The Radius is scaled quadratically.

3.2 Hit selections

To deduce information from the alignment of the first hits of an event, these first hits have to be selected very well so that noise hits are excluded with high confidence. Accordingly, this section addresses hit selections, which were optimized for vetoing strategies.

3.2.1 Local coincidences of two PMTs: L1

Hits on individual PMTs are called PMT hits. The first step of noise reduction is to select only hits with local coincidences. An L1-coincidence is defined as at least two hits on one DOM within a time window (20 ns). Such a coincidence is called a L1 hit. The time of the first PMT hit of the coincidence is taken as the reference time for the L1 hit. In the Letter of Intent [13] an additional requirement is set on the angle between the coincident hit PMTs. If the angle between the hit PMTs is smaller than 90°, it is called a L2 hit. This requirement was not taken in this thesis.

3.2.2 *Causality Clustering*

The next step is to check whether the L1 hits fit to each other globally in the detector. Therefore, the time light needs to travel the distance d between two DOMs is calculated and compared to the time difference Δt between the L1 hits. A time window t_{window} accounts for possible delays due to scattering or calibration uncertainty in arrival time. If $\Delta t > d/c_{\text{water}} + t_{\text{window}}$, it is assumed that there is no causal connection between these L1 hits ($t_{\text{window}} = 50\,\text{ns}$, $c_{water} = 0.217\,\text{m/ns}$). (The chosen timewindow is larger than the typical value in the Letter of Intent [13] making the selection slightly less clean. But this choice works better in the context of the muon veto, as it is essential for the veto to have enough hits in the outer detector part for muon event rejection. So even scattered light hits are wanted to some extent. The final decision if the these hits should be kept, is then made by the *Distance Filter*.) In that way for each pair of L1 hits it is calculated if there is a causal connection, such that clusters of causally connected hits are obtained. All hits that are causally connected with all other hits of the largest cluster pass the selection. This algorithm is therefore called *Causality Clustering*. Many noise hits and hits due to light scattered under large angles can be excluded in that way.

But there is a problem with high energetic muons causing an electromagnetic shower. For explanation of this problem, some definitions are helpful: hits, caused by the muon, are called track hits and hits, caused by the shower, are called track shower hits. Unlike the muon which emits light under the Cherenkov angle, the shower emits light spherically (see Fig. 3.3). In that way light emission backward in the direction of the track occurs such that hits are made later than causality suggests (see Fig. 3.4). If there are more more shower hits than track hits, the *Causality Clustering* algorithm deletes the track hits, because they do not seem to fit the electromagnetic shower hits.

To solve this issue, hits in the outer part of the detector, which are causally connected to at least 40 of the hits selected by *Causality Clustering*, are added again afterwards. Sometimes even this procedure does not bring back the deleted track hits. Therefore, a second *Causality Clustering* of the deleted hits is made and added again if it has more than 10 hits and at least 3 of them are in the vicinity ($d_{max} = 25\,\text{m}$, $\Delta t_{max} = 140\,\text{s}$) of hits of the first *Causality Clustering*.
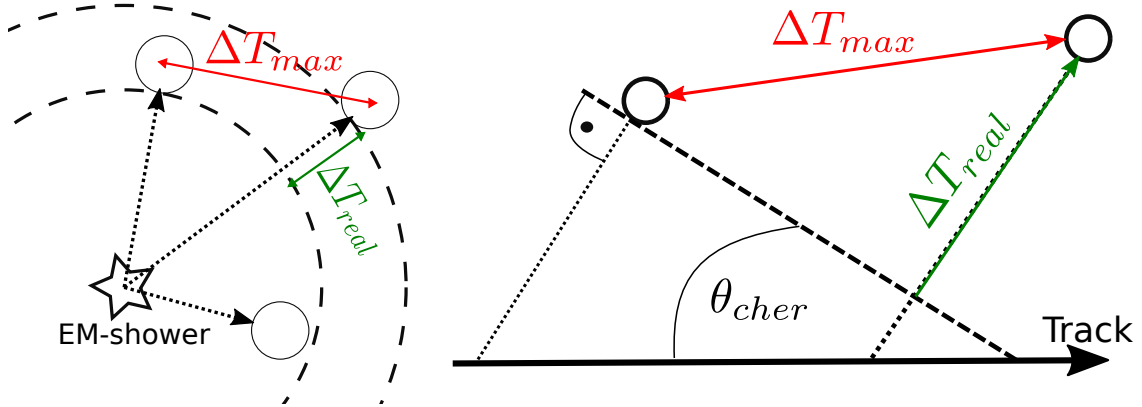
Figure 3.3: A shower (left) emits light from one point in all directions, whereas a track (right) emits light under the Cherenkov angle. In both cases is $\Delta T_{real} < \Delta T_{max}$. - dotted lines: path taken by photon, dashed lines: light fronts, circles: L1 hits, red line: distance between the DOMs and therefore the upper limit for the time difference between them, green line: path that the light takes and therefore really determines the time difference.
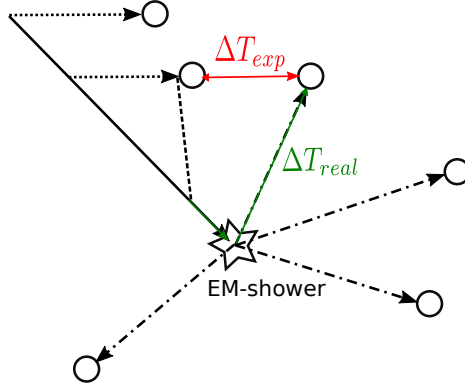

Figure 3.4: A high energetic muon comes in, produces a few track hits and then an electromagnetic cascade. Dotted lines: light path for track hits, dotted dashed lines: light path for shower hits, dashed line: Cherenkov cone at the time of the last track DOM-hit, circles: DOM-hits, red line: distance between a track hit and a backscattered shower hit, green line: path that actually has to be taken to get to that hit; $\Delta T_{exp} < \Delta T_{real}$

3.2.3 Vicinity coincidences: *Distance Filter*

If noise hits are far away from all the other hits in time and distance, they pass the *Causality Clustering*, as the *Causality Clustering* only looks for a relation between time and distance and sets no requirement on their absolute values. To get rid of these noise hits an algorithm is needed that searches for coincidences to L1 hits in their vicinity. In the Letter of Intent [13] the V2L2-coincidence is defined as a coincidence between two L2 hits on different DOMs which are closer than 35 m and within a time window $\Delta t = 10\,\text{ns} + t_d$, where t_d is the time required by the light to travel the distance d between the two DOMs.

But sometimes noise builds up small local clusters of up to 3 L1 hits. Reconstruction algorithm as in the Letter of Intent [13] are not susceptible to such local noise clusters, whereas a muon veto, based on the location of the first hits, is indeed susceptible to those. If the first hits of an event are not selected well, the muon veto will not be functional. Therefore, an algorithm called *Distance*

Filter, which is some kind of V4L1, has been developed.

The *Distance Filter* searches for correlated L1 hits in each L1 hit's vicinity. The vicinity is defined as a sphere of radius $s \sim 24$ m around the hit and therefore spans over some floors (each floor 6 m) of the same string and over direct neighbouring strings (inter-string distance 20 m). Furthermore a pair of L1 hits that are in each other's vicinity should be correlated in time, i.e. the time difference between this pair has to be lower than the time the light needs to travel s ($t = s/c_{\mathrm{water}} = 110$ ns). This means that the time window for each L1 hit within the sphere is the same and is not dependent on the explicit distance between the DOMs. So this is a weaker requirement than in *Causality Clustering*, but as the *Distance Filter* is made to be used after *Causality Clustering* it is sufficient. A further consequence of this requirement is that neighbouring hits are more highly favoured the nearer they are within the sphere. (The time window $\Delta t = t_{\mathrm{add}} + t_d$ is constituted by the actual distance light needs to travel t_d and a additional window t_{add}. If Δt is constant, t_{add} gets larger as t_d gets lower. The larger t_{add} is, the weaker is the requirement.)

If an L1 hit has 3 correlated L1 hits in its vicinity, it is labelled as a 'good hit'. L1 hits which do not satisfy this criterion will be deleted unless they are correlated to such a 'good hit' (see Fig. 3.5). The chosen minimal number of correlated L1 hits in its vicinity is dependent on the number of L1 hits produced in an event, as the mean density of hits drops with the number hits (Tab. 3.1). In that way it is ensured that not too many hits are deleted in events with low luminosity.

number of L1 hits	≥ 10	≥ 5	≥ 2
minimal number of correlated L1 hits	3	2	1

Table 3.1: Chosen minimal number of correlated L1 hits for different numbers of L1 hits produced in an event.
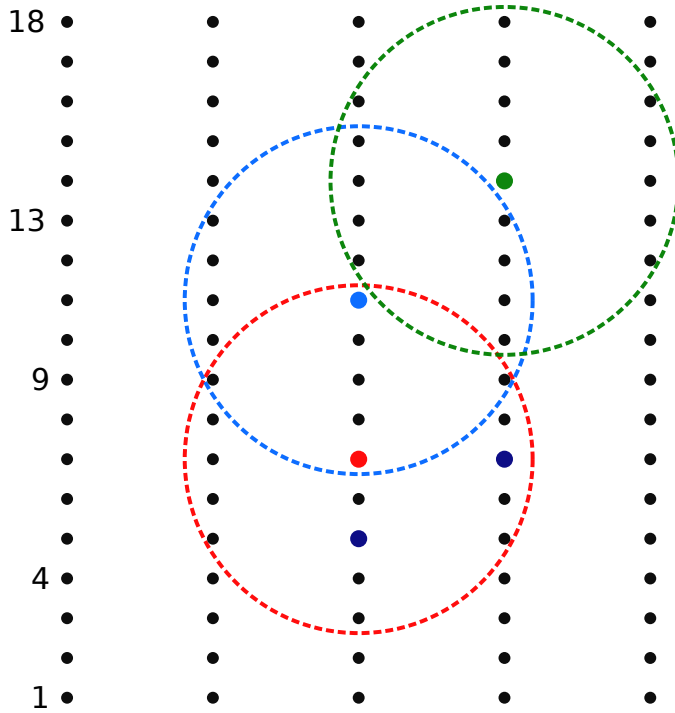

Figure 3.5: *Distance Filter*: The red L1 hit has three L1 hits in its vicinity, hence, it is a 'good hit'.
The light blue hit has only the red hit in its vicinity, but as the red hit is a 'good hit' it is not deleted, whereas the green L1 hit has no L1 hits in its vicinity and thus is deleted.

There is a special treatment of hits at the edges of the detector as those hits mostly have less neighbouring hits and are extremely valuable for the vetoing strategies: as the vicinity sphere of those hits is not completely within the detector, one has to account for this deficit by scaling the radius of the sphere with the factor 1.4. The *upper edge* is defined as the 3 highest floors, the *low edge* as the lowest floor and the *radial edge* as more than 90 % of the maximal radius. If a hit belongs to one of those edges and there are less than 10 hits belonging to this edge, the hit is classified to be an edge hit. If there are already 10 hits in that edge, there are more than enough hits for vetoing and the different treatment would only lead to more noise.

3.2.4 *Dumbbell Rejector*

The *Dumbbell Rejector* searches for events with only two small clusters separated by a large distance (that look like a dumbbell). These events can occur if a muon track only grazes the detector and produces only a few wide spread hits, which are hardly distinguishable from simultaneous random noise hits. Most of these events can be rejected by the *Distance Filter*, but some of them would require to make the *Distance Filter* stronger. This would be accompanied by a loss of low energetic neutrinos, whereas the *Dumbbell Rejector* has a minor effect on the neutrinos and rejects such muon events.

The *Dumbbell Rejector* is only executed if there are ≤ 10 L1 hits and works in the following way. The algorithm sorts L1 hits into local clusters. L1 hits are sorted into the same cluster if their distance is lower than $s = 27$ m and their time difference is lower than $t = s/c_{\text{water}}$. If only two clusters are built in that way and their centres are separated by more than 45 m, the hits belonging to the smaller one are deleted (see Fig. 3.6).

In many cases this procedure is not definite, but these are mainly those cases that do not have the described two cluster structure, therefore the algorithm is then aborted. The *Dumbbell Rejector* was an idea to reject one very specific kind of event and has eventually a minor effect on the veto performance.
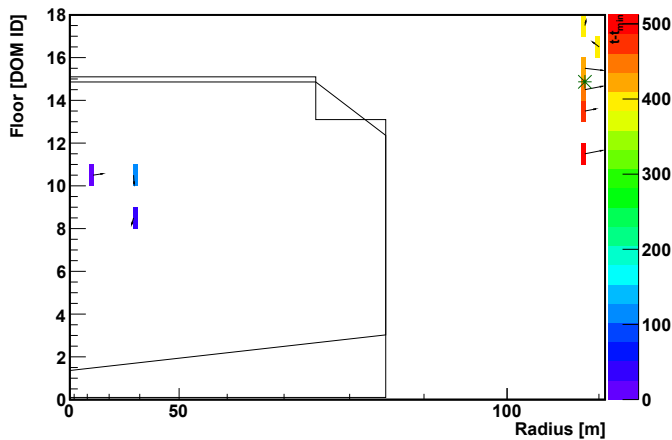

Figure 3.6: *Dumbbell Rejector*: On the left there is a cluster of 3 noise hits obviously unrelated to the cluster on the right. But as the time difference between those clusters is large enough, they passed the *Causality Clustering*. The left cluster could be deleted by *Distance Filter* if no exception for events with low luminosity had been implemented. However, omitting this exception would cause a loss of neutrino events. To prevent this, the *Dumbbell Rejector* explicitly searches for that kind of events with a far lower loss of neutrino events.

3.2.5 Stepwise application of hit selections

The above described hit selections are applied in the following order:

1. Local coincidences (L1): there has to be a local coincidence of at least two PMTs on one DOM within a time window.

2. Weak *Distance Filter*: a L1 hit has to have at least one neighbour L1 hit within 50 m and 250 ns. Most of the hits deleted in this way would even not pass *Causality Clustering*. This step is mainly for event displays and for cases in which the ratio of hits deleted by *Causality Clustering* is important.

3. *Causality Clustering*: the L1 hits have to be causally connected, i.e. the distance between them has to be at least the light travel way. The largest causally connected cluster of hits is chosen.

4. *Causality Clustering* muon optimization: if a muon produces a large em-shower, *Causality Clustering* falsely deletes its track hits. Get the track hits back via a second clustering. This selection has a significant effect on muons, but nearly no effect on neutrinos.

5. *Distance Filter*: a L1 hit has to have 3 other L1 hits within 25 m and 110 ns. The parameters of this selection are adaptive to the number and position of hits.

6. *Dumbbell Rejector*: deletes one of two clusters if there are two clusters separated by a large distance. It is only applied in the case of few hits to account for the weaker *Distance Filter* in that cases. It seldom changes hit selection and its effect is greater for muon events than for neutrino events.

3.2.6 Discussion of example events

Some hit selection behaviour examples are shown in the following event displays (see Sec. 3.1.3 for explanation of used symbols).
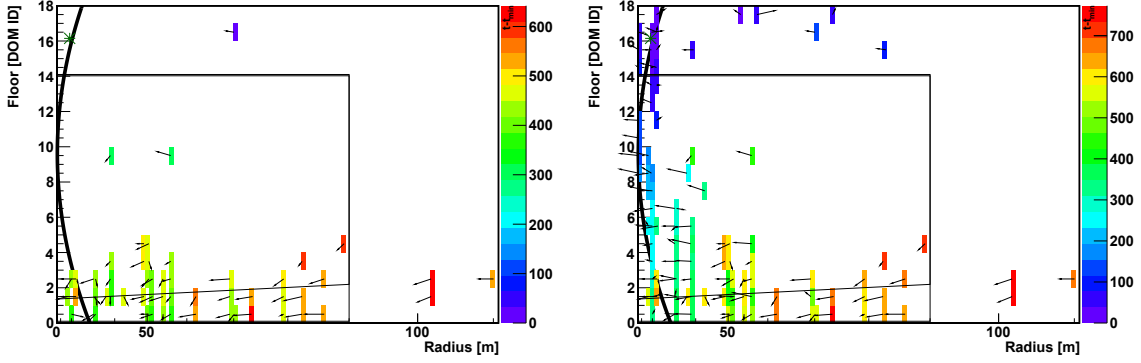

Figure 3.7: Muon causing an em-shower: the track-like part of the event is deleted in the *Causality Clustering* (left) and has to be added again with a second clustering (right)
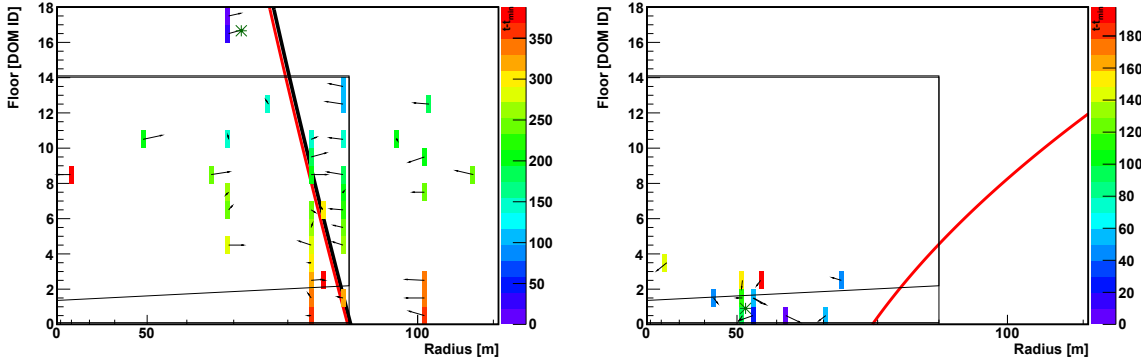

Figure 3.8: There are only two hits in the outer part of the detector within the first $\sim 150\,\mathrm{ns}$, which are very valuable for the veto strategies. These hits would be lost if the *Distance Filter* did not treat them with a larger vicinity sphere radius and time window.

Figure 3.9: Muon flying below the detector producing only a few hits at the bottom of the detector.

3.3 Rejection criteria

3.3.1 Fiducial volume criteria

Most of the rejection criteria reject an event due to the information if something is inside or outside a fiducial volume (Fig. 3.10, Fig. 3.11). To calculate the position of a hit, the position of the DOM is used and not the individual positions of the PMTs within the DOM. In this way it is ensured that all PMTs on one DOM are treated in the same way and no DOM gets bisected by defining the fiducial volume. The normal vector to the photocathode gives the orientation of the PMT and is referred to as 'PMT direction' ($\overrightarrow{PMT}$). All the following criteria have advantages and disadvantages. Sometimes a single criterion cannot give any information about an event. Therefore, a sophisticated connection between them is essential.
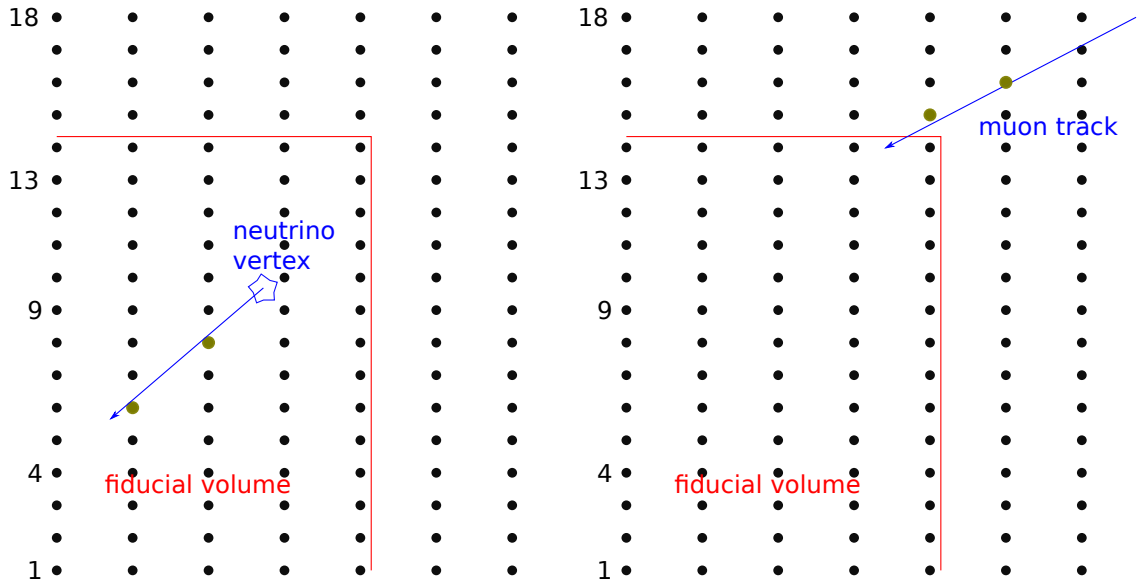
Figure 3.10: Sketch of events to be kept (left) and events to be rejected (right).
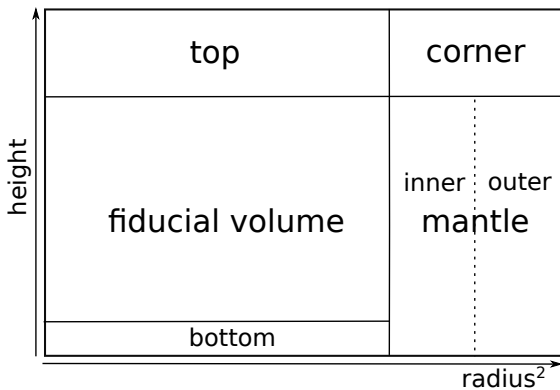

Figure 3.11: Fiducial volume and parts of the detector are shown in radial coordinates. The **top** is given by the upper non fiducial floors and the **mantle** is given by the strings with an great radial distance to the centre of the detector. The intersection of the **top** and the **mantle** is called the **corner** and sometimes the **mantle** is parted in the **inner mantle** and the **outer mantle**. The lowest detector floor is called the **bottom**.

What a muon event looks like depends on whether it is contained (muon track within the detector) or not. Therefore, both cases should be treated differently. Considering the fact that not contained events typically produce less hits than the contained ones, the following definitions are set: An event is defined as having only 'few hits' or 'low luminosity' if the number of L1 hits

$N_{\text{hits}}^{\text{L1}} \leq 10$ and the number of PMT hits $N_{\text{hits}}^{\text{PMT}} \leq 25$ after the final hit selection. In that case the fiducial volume cuts get adjusted (see Sec. 3.3.1) and additional criteria have to be passed (see Sec. 3.3.2).

Outer-criterion: L1 hits in non-fiducial volume and within time margin

A kind of obvious criterion against muons is something like this: if there are hits in the outer part of the detector at the beginning of the event, the particle came from outside. The required number of L1 hits outside the fiducial volume is set to be 2 hits within 105 ns with respect to the first L1 hit. There are difficulties for muons producing only few hits at the beginning and a large em-shower in the centre of the detector. See therefore previous chapter (Sec. 3.2.3), where the hit selection was designed in that way that hits in the outer part of the detector are more likely to be kept. This criterion cannot give any information about the event, if there are not the required number of hits within the time margin in the whole detector. In this case, the criterion is labelled to have a bad accuracy and is ignored.

MeanPos-criterion: mean position of hits within time margin

The *MeanPos*-criterion is a bit more sophisticated: it evaluates more precisely where the first hits of the event were made in the detector. At first, only L1 hits within a time margin, w.r.t the first hit, are selected. The time margin is an input parameter (55 ns) but it is not fixed: if there are less than three L1 hits within this time margin, it is extended, and if there are more than 7 L1 hits within this time margin, it is shortened. The shortening is done because taking more than 7 L1 hits of luminous events would shift the mean position nearer to the centre of the detector. The greatest possible time margin is two times the initial time margin. Then the mean position of selected L1 hits is calculated and weighted by the number the individual PMT hits of the L1 hit. The error is calculated unweighted. The radial part of it is normed on the string distance (20 m) and the vertical part is normed to the inter-DOM distance on a string (6 m). The norm of the error ($\sqrt{x_{\text{err}}^2 + y_{\text{err}}^2 + z_{\text{err}}^2}$) is an estimation of the spread of the hits, which is mainly independent of the detector geometry. If the norm of the error is greater than 1.7, the criterion is labelled to have a bad accuracy.

As the mean position is computed only from few L1 hits, each L1 hit has a significant impact on the resulting mean position and its error. To reduce this susceptibility to noise, outliers are ignored: for each of the selected hits the mean position and standard error without the questionable hit (and without the described normalization) is calculated. If the distance between the position of the questionable hit and the new mean position is more than 4 times the new standard error, the hit is classified as an outlier. If less than 30 % of the selected hits are outliers, the outliers are deleted. Elsewise the hits are quite dispersed and the outlier definition makes no sense, therefore, no hits are deleted.

The cut on the mean position is made in radial coordinates via a polygonal shape. Two different shapes are considered dependent on the number of hits (Fig. 3.12, Fig. 3.13). In 'normal' muon events, muons enter the detector from above or in radial inward direction. Therefore, the distribution of the mean position is mainly populated at the **top** and at the **mantel**. These 'normal' muon events are described by many hits and good accuracy (Fig. 3.12). The volume

enclosed by the cut is $1.87 \cdot 10^6 \, \mathrm{m}^3$. On the other hand, muons with tracks outside the detector only cause a few dispersed hits within the detector ('low luminosity' events). The distribution of the mean position changes: less positions at the **top**, whereas more at the **mantel** and at the **bottom** (Fig. 3.13). The cut chosen in this case encloses a volume of $1.69 \cdot 10^6 \, \mathrm{m}^3$.
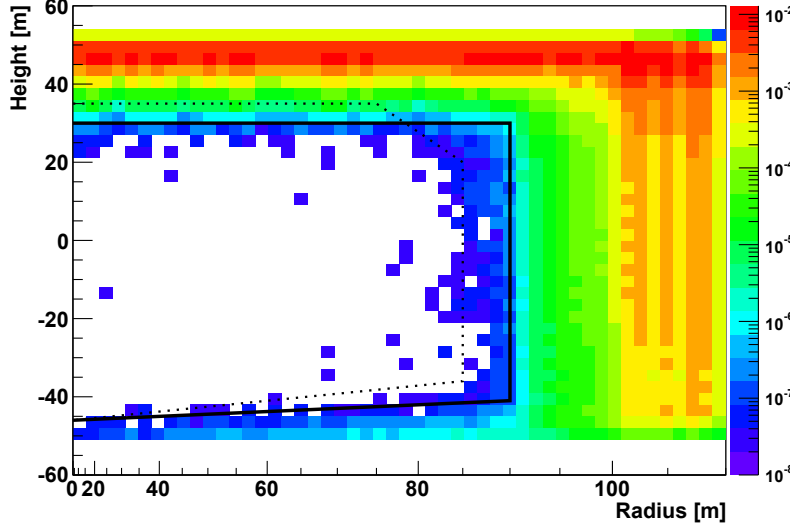

Figure 3.12: Mean position of luminous 'normal' muon events: the Distribution is peaked at the **top** and at the **mantel**. The contour of the chosen cut is shown as a black line. The histogram is normalised such that the total rate, the sum of all entries, is 1.
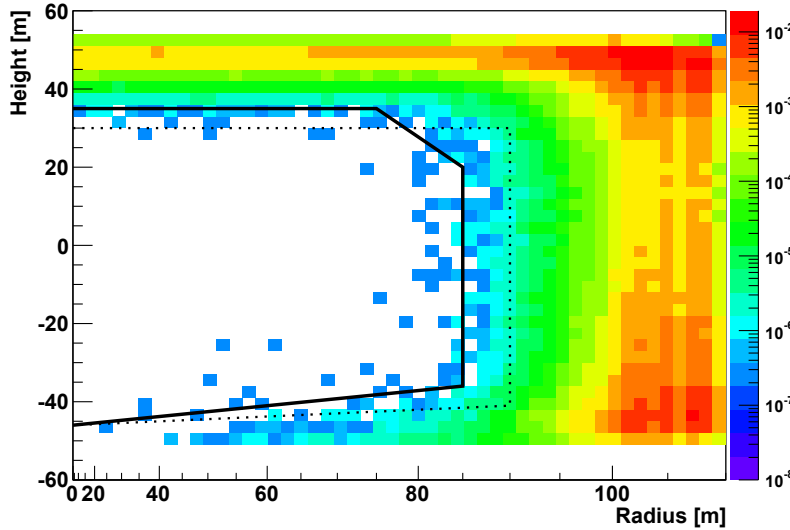
Figure 3.13: Mean position of low luminosity muon events: less positions are at the **top**, however, there are more at the **mantel** and at the **bottom** detector part. The contour (black line) of the chosen cut as well as the cut for the normal case are shown in comparison. Events excludable by N_{hits}-rejection-part were ignored. The histogram is normalised such that the total rate is 1.

For analysis reasons there is even a weaker cut on the mean position of hits (weak *MeanPos*-criterion). This one is independent of the number of hits and has no lower border. Furthermore its height is 10 m higher and its radius 5 m larger compared to the 'normal' cut.

The mean position of neutrino events is nearly uniformly distributed (see Fig. 3.14). A small excess is seen at the **top** and at the **mantel**. This is caused by neutrino events with vertexes outside the detector. Further deviations of a uniform distribution are caused by the detector geometry.
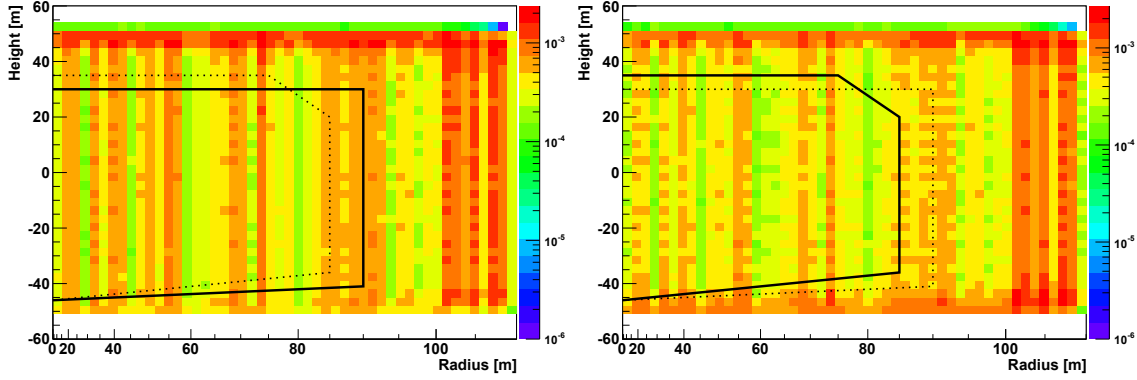
Figure 3.14: Mean position muon neutrino events: normal events (left) and low luminosity events (right). Events excludable by N_{hits}-rejection-part were ignored. The histogram is normalised such that the total rate is 1.

MeanDir-criterion: mean direction of hits within time margin

Another idea is to use the directional information of the PMT hits: if there are hits outside the fiducial volume but they are caused by an event inside of it, they should point towards the surface of the fiducial volume (inward). As for the *MeanPos*-criterion only L1 hits within a time margin, w.r.t the first hit, are selected. The time margin is an input parameter (125 ns) that gets extended if there are less than 8 PMT hits within the initial time margin. The greatest possible time margin is 1.5 times the initial time margin. For L1 hits at the **top**, the angle between upward $\hat{e}_z$ and PMT direction $\overrightarrow{PMT}$ is calculated for each PMT. Whereas for the **mantel**, the angle between radial outward $\hat{e}_r$ and PMT direction is computed. The L1 hits in the **corner** are only counted but no angle is calculated because an inward direction is not well defined for this part. If there are enough hits in the inner mantel, hits in the outer mantel are ignored. Elsewise hits in the inner and outer mantel are treated together (see Fig. 3.15 for explanation).
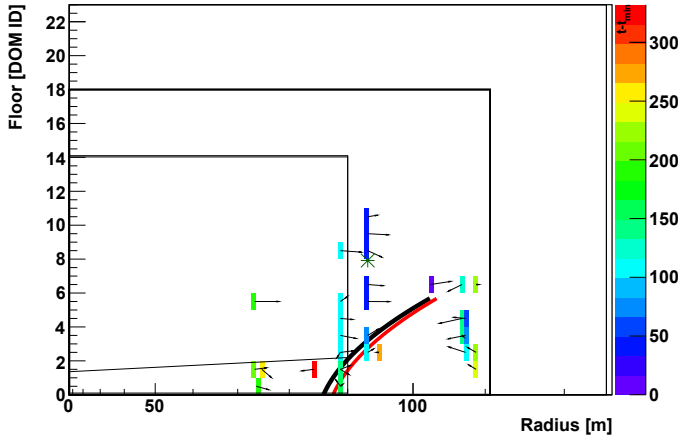

Figure 3.15: If a muon goes down within the radial outer part, it produces hits pointing inward (outer mantel) and outward (inner mantel). Therefore, if there are enough hits in the **inner mantel**, the use of their mean direction is more reliable than the use of the mean direction of all hits in the **mantel**.

For the hits in the **mantel** and for the hits at the **top** the mean value of the cosine of their angles as well as the standard error on it are calculated. As for *MeanPos*-criterion, outliers are ignored: for each of the selected hits the mean direction and standard error without the questionable hit is calculated. If the cosine of the angle between the direction of the questionable hit and the new mean direction is more than 6 times the new standard error, the hit is classified as an outlier. If less

than 20 % of the selected hits are outliers, the outliers are deleted. Elsewise the outlier definition makes no sense, therefore, no hits are ignored.

For reminder, the cosine of the angle between two normalized vectors, $\overrightarrow{\text{PMT}}$ and $\hat{e}_{r,z}$, is given by: $\overrightarrow{\text{PMT}} \cdot \hat{e}_{r,z}$. At first, it is individually decided for the **top** and for the **mantel** if the event passes: the mean cosine has to be lower than -0.3 (pointing inward) and the standard deviation has to be lower than 0.4 (no great spread). If there are less than 5 PMTs in the part in question, the event passes regardless of the mean and deviation values. Then it is decided if the event passes in both parts, which implies a logical AND between both parts with the additional restrictions:

1. not in both parts are less than 5 PMT hits unless in both are zero PMT hits

2. there have to be less than 2 L1 hits in the **corner**

Fig. 3.16 shows the distribution of $\overrightarrow{\text{PMT}} \cdot \hat{e}_z$ vs $\overrightarrow{\text{PMT}} \cdot \hat{e}_r$. If there are less than 5 PMT hits in one of both parts (**top** or **mantel**), the corresponding direction is shown as -1. Events excludable by *MeanPos*-rejection-part and N_{hits}-rejection-part were ignored in this plot. In most neutrinos events the hits outside the fiducial volume point inwards, whereas those of muon events do not.

The outcome of this criterion is then used in the *Connect*-criterion (see Sec. 3.3.3) in a logical OR to the *Outer*-criterion. Not just evaluating the number of hits outside the fiducial volume, like in the *Outer*-criterion, but even evaluating whether these hits were caused by an event inside of the fiducial volume, like in *MeanDir*-criterion, gives a better neutrino detection efficiency.
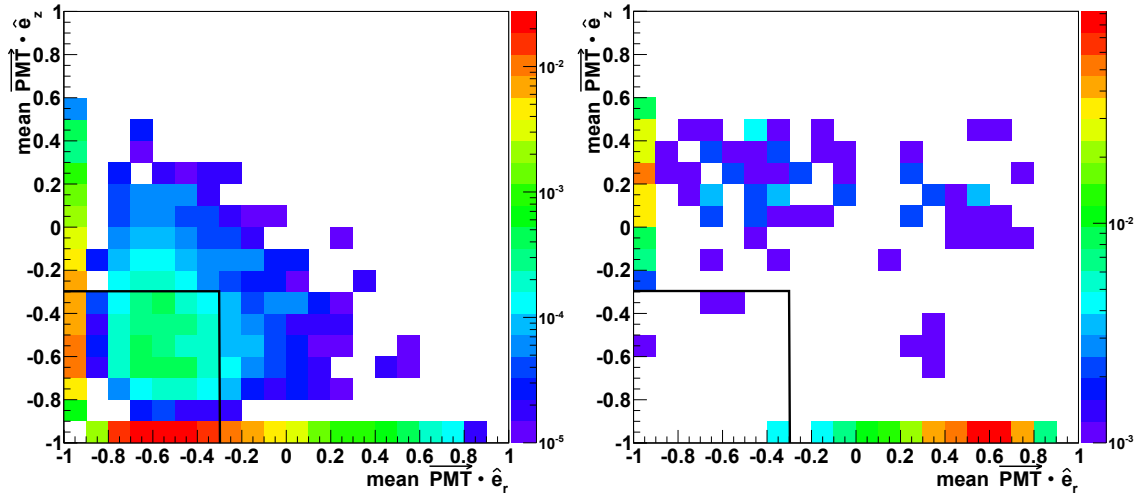

Figure 3.16: Distribution of $\overrightarrow{\text{PMT}} \cdot \hat{e}_z$ vs $\overrightarrow{\text{PMT}} \cdot \hat{e}_r$ for events in which not both parts have less than 5 PMT hits. If a part has less than 5 hits, its mean cosine is set to -1. In that way events can be shown of which only the direction in one of the parts is obtainable. The point (-1,-1) is not shown as it contains too many neutrino events. Events excludable by *MeanPos*-rejection-part and N_{hits}-rejection-part were ignored. In most neutrinos events (left) the hits outside the fiducial volume point inwards, whereas those of muon events (right) do not. The contour of the chosen cut is shown in black.

3.3.2 Criteria against events with dispersed hits: N_{hits}-rejection-part

In the case of 'low luminosity' events, the adjustment of the fiducial volume is sometimes not sufficient to reject muons. Therefore, other criteria have to reject events characterised by very few

dispersed hits produced by muons which are only grazing the detector.

At first the characterization of 'dispersed hits' is addressed: as described in Sec. 3.2.3 the *Distance Filter* selects hits with vicinity coincidences. Per definition events with dispersed hits have less vicinity coincidences than normal events, therefore more hits get deleted by the *Distance Filter*. Thus the fraction of hits passing the *Distance Filter* gives an estimation of how dispersed the hits are. The lower the fraction is, the more dispersed the hits are. A good cut is found to be 0.6 (see Fig. 3.17). But as the less hits an event has, the less vicinity coincidences the *Distance Filter* requires, the requirement on the fraction is insufficient for events with very few hits. Therefore, those events have to be rejected in another way: if an event has less than 5 L1 hits after the last hit selection, a requirement on the number of PMT hits is set: $N_{\text{hits}}^{\text{PMT}} > 5 \cdot \sqrt{N_{\text{hits}}^{\text{L1}}}$ (see Fig. 3.18). This means that events with very few L1 hits have to have many PMT hits on each DOM.
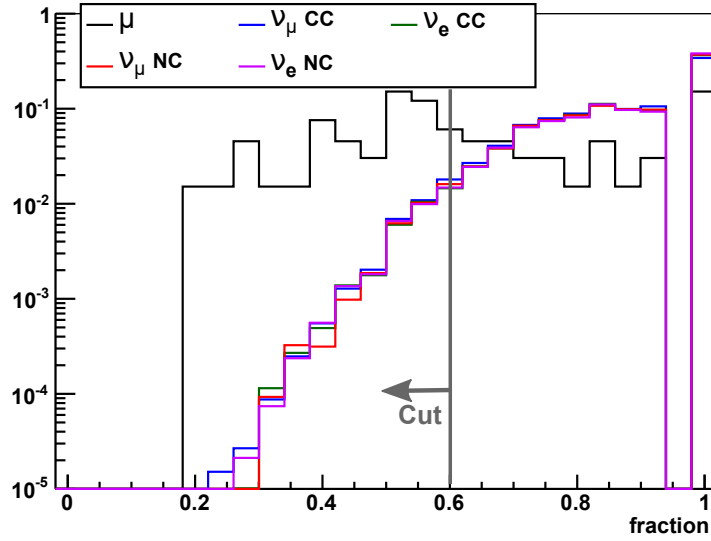
Figure 3.17: To reject events with dispersed hits, the fraction of hits passing the *Distance Filter* has to be greater than 0.6. Events excludable by *MeanPos*-rejection-part and *Outer*-rejection-part were omitted and the restriction of Fig. 3.18 was already applied.
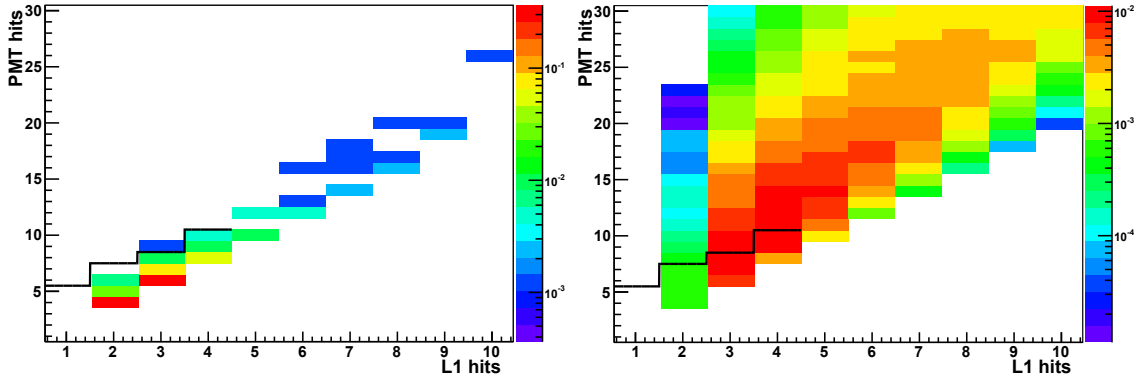
Figure 3.18: The number of PMT hits is plotted against the number of L1 hits for muon (left) and neutrino (right) events. The histograms are normalised such that the total rate is 1. Events with less than 5 L1 hits have to satisfy: $N_{\text{hits}}^{\text{PMT}} > 5 \cdot \sqrt{N_{\text{hits}}^{\text{L1}}}$ (shown as black line). Events excludable by *MeanPos*-rejection-part and *Outer*-rejection-part were omitted.

3.3.3 Connection of criteria

The *Connect*-criterion is a logical connection of the previously described criteria. For a better understanding it has been decomposed in rejection-parts connected with an logical AND. These parts are illustrated in the diagram Fig. 3.19. See Appendix A for criteria that were studied but not used.
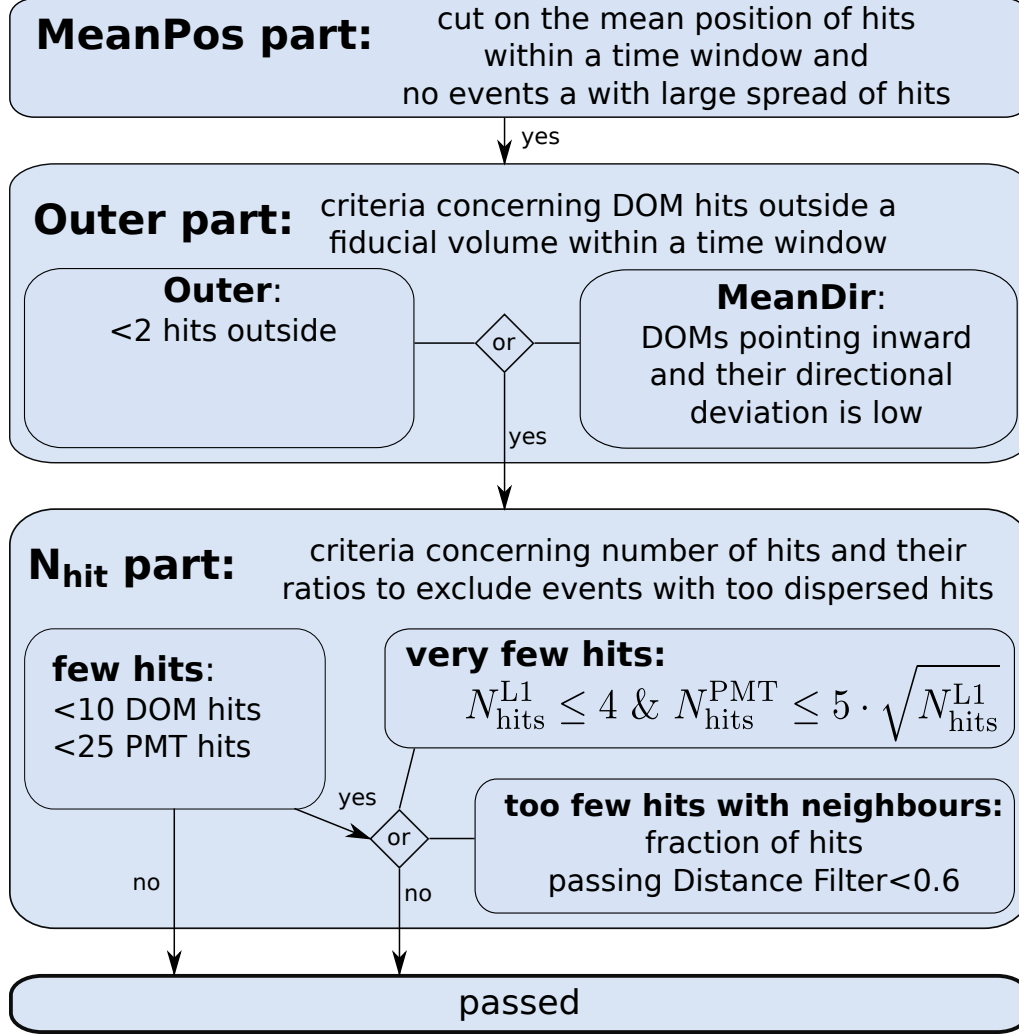

Figure 3.19: The muon veto decision tree consists of three rejection-parts, which are connected via a logical AND: *MeanPos*-rejection-part, *Outer*-rejection-part and N_{hits}-rejection-part.

3.3.4 Criteria based on reconstruction

All the following methods are based on a log-likelihood maximisation for reconstructing the direction of the track. This procedure is called 'track fitting'. Those fits are performed with the FilteringFit algorithm [22] within SeaTray. This algorithm scans the whole phase space by generating a discrete number of isotropically distributed track hypotheses. In that way prefit candidates are obtained. For each track candidate direct track hits, i.e. hits that fit to be produced by this track, are selected. These hit selections are added up and the final track fit is executed. Although it is a track fitting algorithm, it is also used for the shower-like events (ν_e CC and NC) to be independent from shower-like/track-like classification. Rejection criteria based on event reconstruction, short 'reco-criteria', are more computational time consuming than the before described 'non-reco-criteria'.

Fit quality

The quality parameter Λ is defined as the log-likelihood per degree of freedom:

$$\Lambda = \frac{\log L}{N_{\mathrm{d.o.f.}}} \tag{3.1}$$

whereby the number of degrees of freedom $N_{\mathrm{d.o.f.}}$ is given by the number of hits minus the number of fit parameters: $N_{\mathrm{d.o.f.}} = N_{\mathrm{hit}} - 5$.

This quantity takes negative values and is larger (i.e. closer to zero) for better reconstructed tracks.
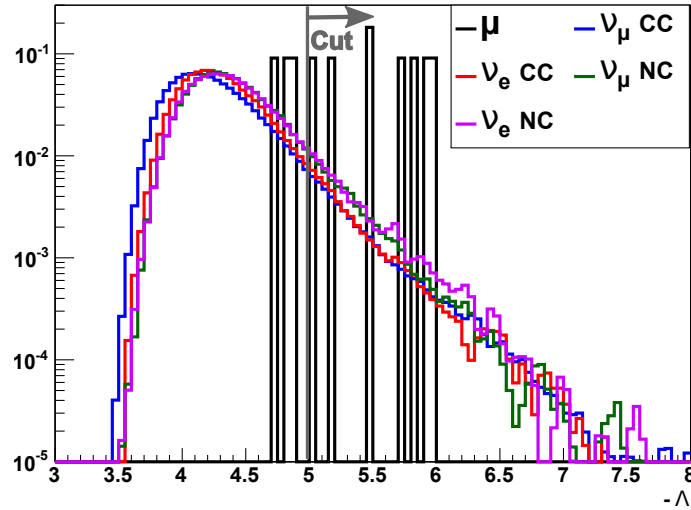
Figure 3.20: Fit quality Λ of events with only 'few hits' that passed all other rejection criteria. A cut at $\Lambda = -5$ (grey line) is chosen to exclude muon events (black).

Fig. 3.20 presents the fit quality distribution of events with only 'few hits' (definition see Sec. 3.3.1) that additionally passed the *Connect*-criterion and the cut on the reconstructed track starting point, which is described in the next section. By requiring a fit quality of at least $\Lambda = -5$, most of the remaining muon events can be excluded. Regarding neutrino events, the median fit quality of shower-like events is slightly worse than for track-like events, as it is the false event

hypothesis. However, the impact of this fact on the neutrino effective volume of shower-like events is low.

Track starting point

Hits are back-projected under the Cherenkov angle θ_C onto the track to determine the emission point of the photon (see Fig. 3.21). The track starting point is then the emission point of the first detected photon.
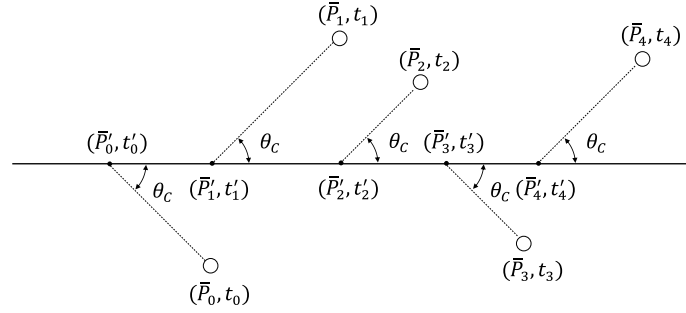

Figure 3.21: Hits (open circles) are back-projected under the Cherenkov angle θ_C onto the track (horizontal arrow). Taken from [13].

Muons typically have reconstructed track starting points outside of the detector (Fig. 3.22), whereas the track starting point of neutrinos is mostly reconstructed to be inside the detector (Fig. 3.23). Such that most of the remaining muon events can be excluded by placing a cut on it in cylindrical coordinates. Events with bad fit quality were omitted in all plots.

The reconstruction was executed if a weaker than normal cut on the mean position of hits (weak *MeanPos*-criterion) was passed (see Fig. 3.24 left). In that way it was possible to analyse where the reconstructed track starting point of the events, which have passed specific criteria, lies. The weak *MeanPos*-criterion reduces the number of track starting points above and radial outside of the detector (compare Fig. 3.24 left to Fig. 3.22 left). Criteria on the number of hits (N_{hits}-rejection-part) primarily exclude events with track starting points reconstructed in the radial outside area (see Fig. 3.24 right). The cut on the mean position of hits (*MeanPos*-rejection-part) mainly let pass track starting points which are above the detector (see Fig. 3.24 left). The criteria on the number of hits and mean direction of hits in the outer detector part (*Outer*-rejection-part) mainly let pass track starting points which are below the detector (see Fig. 3.24 right), because they do not care about hits at the bottom of the detector as the *MeanPos*-criterion does.
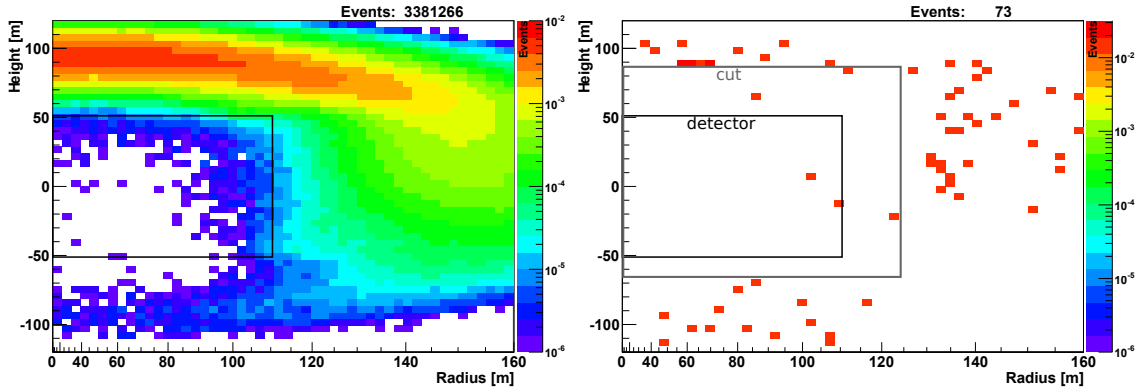
Figure 3.22: Reconstructed track starting point of muon events: without veto criteria (left) and with *Connect*-criterion (right). For the left plot only 7 % of the full event sample was chosen.
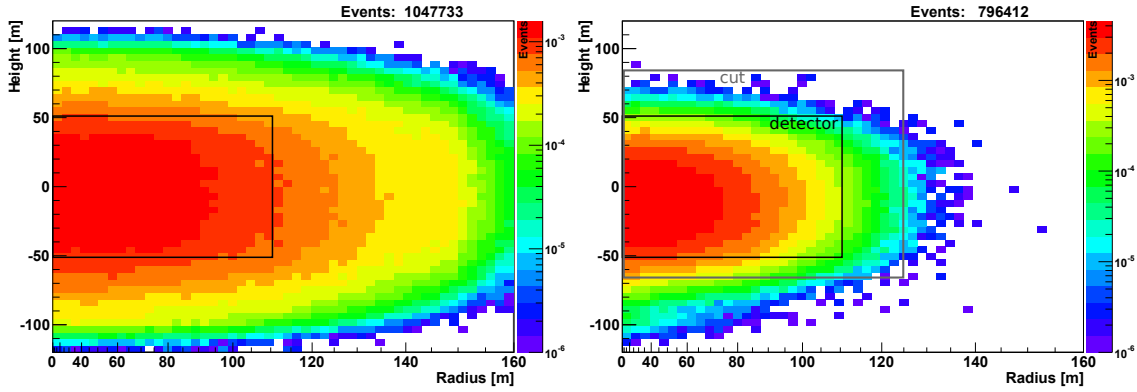

Figure 3.23: Reconstructed track starting point of neutrino events: without veto criteria (left) and with *Connect*-criterion (right). For the left plot only 33 % of the full event sample was chosen.
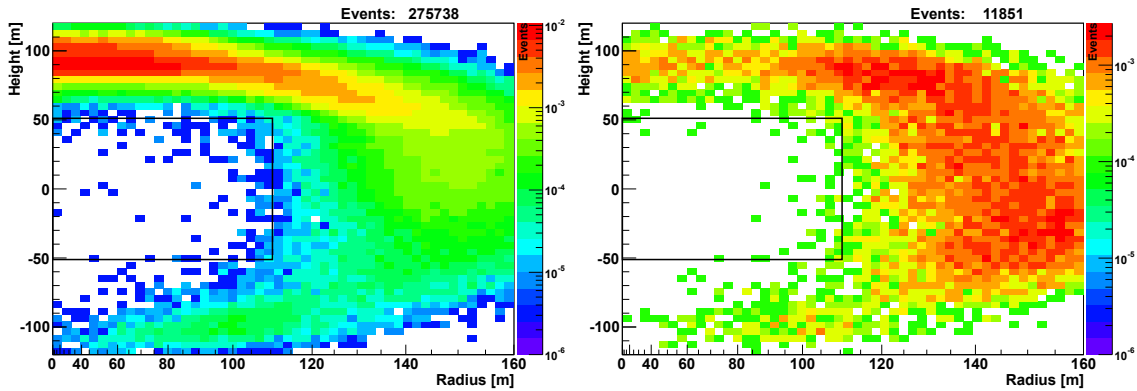

Figure 3.24: Reconstructed track starting point of muon events: events passing weak *MeanPos*-criterion (left) and events rejected by N_{hits}-rejection-part (right).
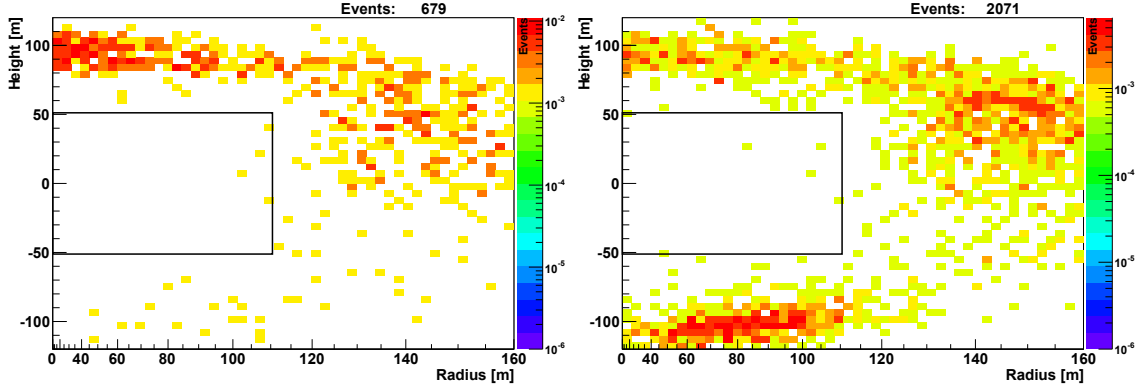
Figure 3.25: Reconstructed track starting point of muon events: events passing *MeanPos*-rejection-part (left) and events passing *Outer*-rejection-part (right).

3.3.5 Discussion of example events

In total, $15 \cdot 10^6$ muon events were simulated, which equals a livetime of half a month. Only ~ 100 out of these events passed all non-reco-criteria (*Connect*-criterion) and only 5 passed all criteria. Some of those events are shown in the following event displays (see Sec. 3.1.3 for explanation of used symbols).
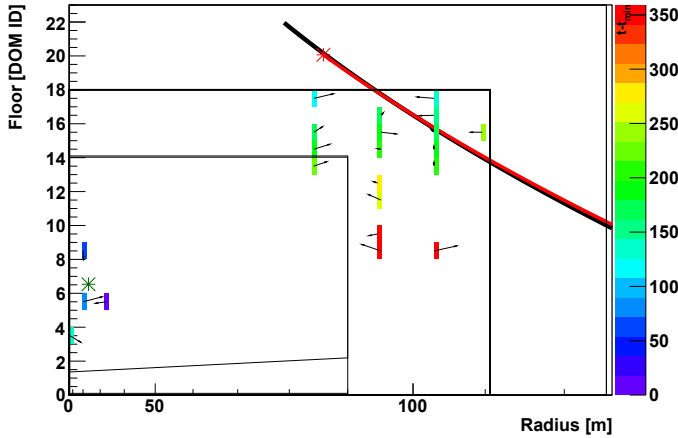
Figure 3.26: Passed all criteria: the first 4 hits are in this case noise hits which are in a local cluster in the centre of the detector far away from the real event at the top. The *Causality Clustering* only deletes clusters of up to 3 hits and the *Dumbbell Rejector* only works for events with few hits. As *MeanPos*-criterion, *MeanDir*-criterion and *Outer*-criterion only consider hits during a time window since the first hit, none of them can do anything. Furthermore even the reconstruction of the track starting point is too near to the detector.
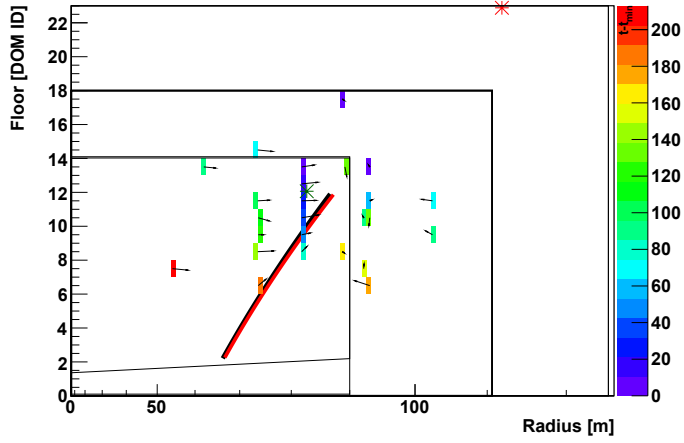
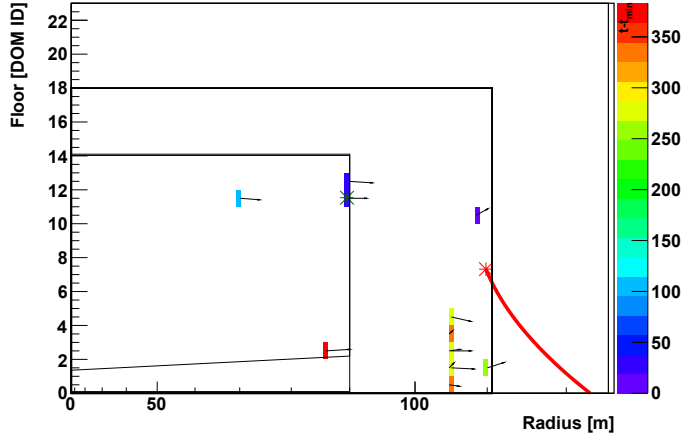Figure 3.27: Passed all criteria: too few hits in the outer part of the detector.

Figure 3.28: Passed all criteria: dispersed hits that could not be characterized by *NHitPart*. A criterion on the mean direction of the hits without time window could be used for rejection, but such a criterion would be accompanied by a distortion of the neutrino effective mass E-$\cos\theta_z$-plane (see Sec. A).

3.4 Muon Veto Results

3.4.1 Contamination and efficiency

The following section deals with the interaction rate, which is defined as the detected number of interactions per unit time. The interaction rate is estimated by a Monte Carlo simulation of muon and neutrino events (see Sec. 2.6). 7000 muon files are used with a livetime of $\sim 3\,\text{min}$ each, which makes a total equivalent livetime of about half a month.

The muon contamination is defined as $\mu_{\text{con}} = R^\mu_{\text{pass}}/R^\nu_{\text{pass}}$, where R^μ_{pass} is the muon rate passed through fiducial criteria and R^ν_{pass} is the passed neutrino rate, respectively. For muons, a suppression $\mu_{\text{sup}} = R^\mu_{\text{pass}}/R^\mu_{\text{tot}}$ and for neutrinos an efficiency $\nu_{\text{eff}} = R^\nu_{\text{pass}}/R^\nu_{\text{tot}}$ can be defined, whereby R_{tot} stands for the total rate. The relation between efficiency and effective mass was outlined in Sec. 2.7. In this section the contamination and effective mass are averaged over energy and zenith angle with interaction rate weightings.

For the suppression/efficiency Bayesian statistics [3] are used to estimate asymmetric $1\,\sigma$ errors. The errors on the contamination can then be obtained by error propagation. This is carried out independently for the upper and lower errors (no error on total rate R_{tot} is assumed):

$$\mu_{\text{con,err}} = \mu_{\text{con}}\sqrt{(\mu_{\text{sup,err}}/\mu_{\text{sup}})^2 + (\nu_{\text{eff,err}}/\nu_{\text{eff}})^2}. \tag{3.2}$$

The rejection parts (see Fig. 3.19) and reco-criteria (see Sec. 3.3.4) are successively applied. The contamination is plotted against the effective mass for each step and for different neutrino interaction types (see Fig. 3.29 and Fig. 3.30). For $\overset{\leftrightarrow}{\nu}_\mu$ CC-interactions the first rejection by the *MeanPos*-rejection-part achieves a contamination of 2.6, then the *Connect*-criterion lowers it to 0.12 and by applying the reco-criteria additionally the contamination drops to 0.006. The different contamination for the other interaction types is mainly due to the different rates. However, the different turnon behaviour affects the mean effective mass (see Fig. 3.31). For a more detailed discussion of combining the rejection criteria see Appendix B.
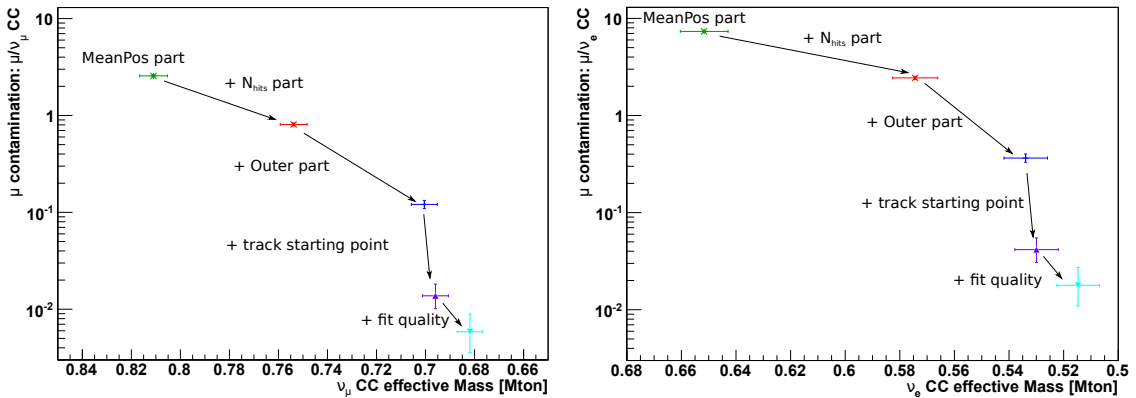

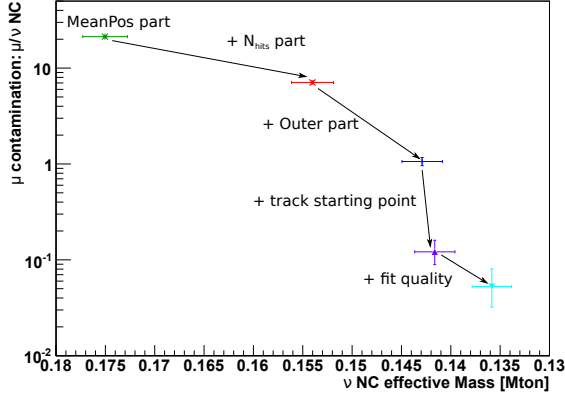Figure 3.29: Contamination vs effective mass averaged over energy and zenith angle (only down-going events: $\cos\theta_z > 0$) for step by step application of rejection parts - left: ν_μ CC, right: ν_e CC.

---

[3]https://root.cern.ch/doc,TGraphAsymmErrors::BayesDivide

Figure 3.30: Contamination vs effective mass averaged over energy and zenith angle (only downgoing events: $\cos\theta_z > 0$) for step by step application of rejection parts - ν NC.
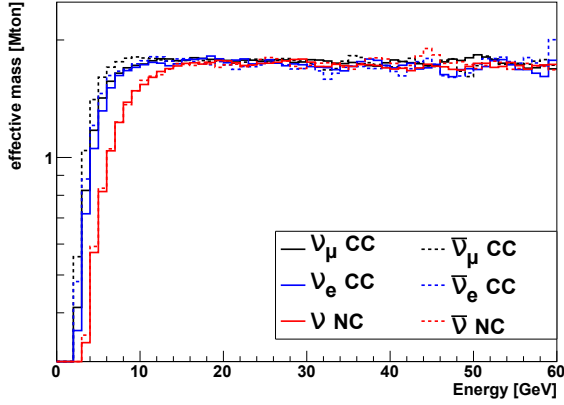
3.4.2 Energy and zenith dependency of effective mass

Figure 3.31: Energy dependency of effective mass averaged from $\cos\theta_z = 0$ to $\cos\theta_z = 1$: nearly constant above 10 GeV.
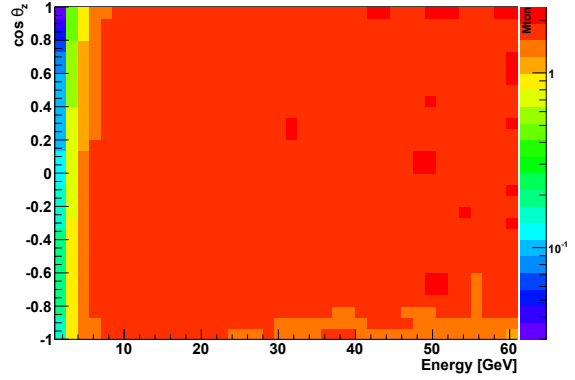
Figure 3.32: Energy and zenith angle dependency of effective mass as 2D plot. The plot shows ν_μ CC-interactions as example, but the plots for antineutrinos and other interaction types look similar. The distribution is nearly independent of $\cos\theta_z$. Only a slight deficit in effective mass for $\cos\theta_z \sim -1$ at high energy can be seen.

The effective mass is nearly constant above 10 GeV, whereby the NC-interactions have a bit greater extended turnon range than CC-interactions (see Fig. 3.31). Furthermore, the effective mass only shows a minor zenith angle (θ_z) dependency: at high energies, there is a slight deficit in effective mass for an zenith angle of $\cos\theta_z \sim -1$, which corresponds to upgoing neutrinos (see Fig. 3.32). This is caused by the cut in reconstructed starting track position, maybe further optimisation could reduce this anomaly. But as this muon veto is only intended for downgoing neutrinos, this can be neglected. Tab. 3.2 shows the effective mass above 10 GeV for CC events and above 15 GeV for NC events, respectively. The effective mass at saturation is about 1.75 Mton, which equals about 44 % of the instrumented volume ($3.9 \cdot 10^6\,\mathrm{m}^3$).

Table 3.2: Effective mass/volume at saturation for each interaction.

interaction	ν_μ CC	$\overline{\nu}_\mu$ CC	ν_e CC	$\overline{\nu}_e$ CC	ν NC	$\overline{\nu}$ NC
effective mass [Mton]	1.81 ± 0.02	1.79 ± 0.02	1.74 ± 0.02	1.78 ± 0.03	1.75 ± 0.02	1.76 ± 0.03
effective volume [$10^6\,\mathrm{m}^3$]	1.76 ± 0.02	1.74 ± 0.02	1.69 ± 0.02	1.74 ± 0.03	1.71 ± 0.02	1.71 ± 0.03

3.4.3 Energy dependency of muon contamination

As only 5 muon events passed all criteria, it is impossible to make a statistical meaningful E-$\cos\theta_z$-plot. To get more statistics, a weaker combination of criteria is chosen: the cut on the mean position is loosened, the *Outer*-criterion and *MeanDir*-criterion are ignored, whereas the N_{hits}-rejection-part as well as the reco-criteria are applied unmodified. Furthermore, as reconstructed energy of muons and neutrinos could differ, the number of hits distribution after the *Causality Clustering*, which is some kind of energy estimator, is chosen for a comparison instead of the energy distribution.
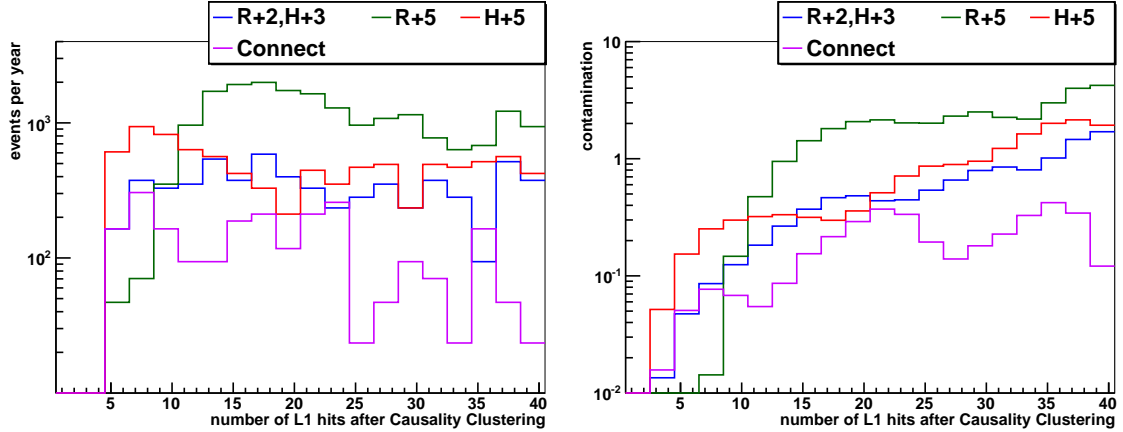
Figure 3.33: Energy dependency of muon contamination: muon flux (left) and muon contamination (right) as function of the number of L1 hits after the final hit selection. A smoothing was applied on the right histogram to account for statistical variations.

By weakly enlarging the fiducial volume of the *MeanPos*-criterion both in height and radius one gets a mainly constant number-of-L1-hit-distribution of muon events. This means that the contamination increases with the number of L1 hits as the neutrino rate falls. When only scaling the radius, the contamination for more than 10 L1 hits is increased. However, only increasing the height results in a muon contamination enhancement at low number of L1 hits ('few hits' regime) and at high number of L1 hits (>35).

The slightly higher contamination at high energy is caused by the fact that atmospheric muons are usually more energetic than neutrinos. Therefore, one would need a greater suppression at high energies than at low energies. For comparison, the neutrino rate has its maximum at 8 L1 Hits ($7\cdot10^3$ events per year) and falls about one order of magnitude towards 40 L1 Hits. In the binning of Fig. 3.33, one muon event with 40 L1 Hits results into a contamination of about 0.1 in the bin in question.

3.4.4 Conclusion

The muon veto was optimised and evaluated for a 6 m vertical detector spacing. It uses a kind of fiducializing as it is used in similar detectors, i.e. the pattern of the first hits of an event gives information about whether the event started outside a fiducial volume or not. At first a very clean hit selection was developed to be confident that the hits, from which the information is deduced, are not just noise hits (i.a. *Causality Clustering* and *Distance Filter*). Then various parameters describing the pattern of the first hits are calculated and cuts are applied (i.a. *MeanPos*-rejection-part and *Outer*-rejection-part). Events from which no reliable information can be deduced are classified by the N_{hits}-rejection-part. By these criteria already a contamination by atmospheric muons of less than 15 % is achieved. Finally, full reconstruction is applied and cuts on calculated parameters are placed (i.a. track starting point). This decreases the contamination further to about 1 %. The effective mass for downgoing neutrinos after the muon veto cut is roughly about 1.75 Mton for the neutrino energy regime above 10 GeV, which corresponds to about nearly 50 % of the instrumented volume.

Chapter 4

Flux investigations

Having obtained the efficiency for detecting downgoing neutrinos (Sec. 3.4.2), investigations on the precision of a downgoing neutrino flux measurement can be made. For simplicity no flavour separation is assumed and only muon and electron (anti-)neutrino fluxes are used. In the following E refers to the neutrino energy and θ_z to its zenith angle, as far as not otherwise referenced.

4.1 Theoretical neutrino flux

Neutrino flux calculations were made by various groups [16, 23, 24] based on the detected muon flux and hadronic interaction models calibrated by accelerator data. The latest and most sophisticated calculation is HKKM15 [25]. Accordingly, this work uses the flux calculation of HKKM15 for the Frejus site (without a mountain over the detector at solar-minimum), which corresponds to the flux at ORCA site to good approximation. The flux is averaged over the azimuth angle.

Some peculiarities of this flux were plotted for discussion. The neutrino flux mainly follows a power-law in energy $N(E) \propto E^{-\gamma}$ with the spectral index $\gamma \sim 3$ in the relevant energy regime (Fig. 4.1) as the primary cosmic ray flux does (Sec. 2.1). The explicit index is dependent on the flavour. Fig. 4.2 shows the $\cos\theta_z$-dependency: the ratio horizontal ($\cos\theta_z \sim 0$) to up- or downgoing ($|\cos\theta_z| \sim 1$) is about 2. Furthermore the flavour ratios (Eq. 2.2, Fig. 4.3) are quite important as they reflect the properties of the interaction producing the neutrinos.

Uncertainties of flux parameters were evaluated by the Bartol-Group in 2006 [34] and the energy dependent uncertainty was recently re-evaluated by [35]. In the relevant energy range around $10\,\mathrm{GeV}$ the uncertainty dropped by about $40\,\%$ due to better measurements in the last decade (see Fig. 4.4). In both evaluations the uncertainties on the initial cosmic ray fluxes and the uncertainties on the atmospheric interactions were tracked through the simulation of the resulting neutrino flux. The neutrino flavour ratios have lower uncertainty than the overall flux, because some sources of uncertainty cancel each other out (see Fig. 4.5). This is especially the case for the $(\nu_\mu + \overline{\nu}_\mu)/(\nu_e + \overline{\nu}_e)$ ratio, which has only an uncertainty of around $1\,\%$. Fig. 4.6 shows the ratios of horizontal to upgoing $\cos\theta_z$, which are quite low, too. To conclude, the overall uncertainty on the flux normalisation is about $15\,\%$, whereas shape and neutrinos flavour ratios are widely known.
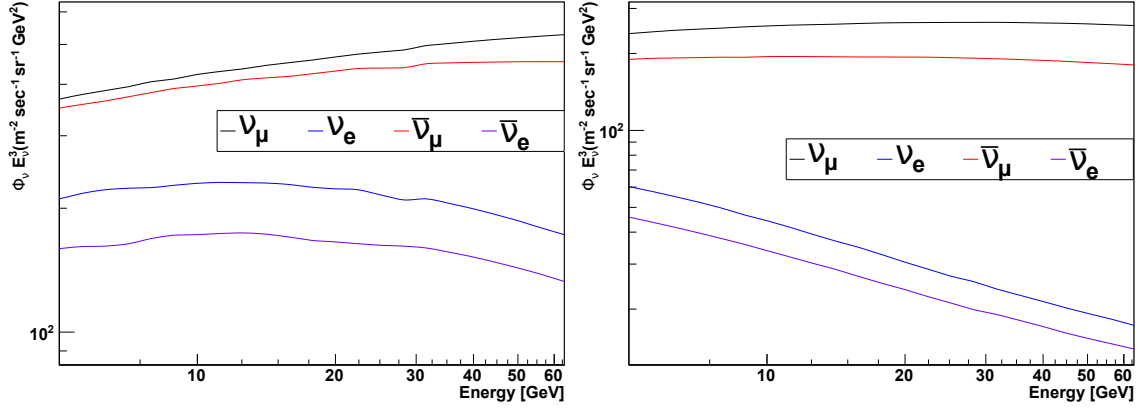
Figure 4.1: The energy slope of the neutrino flux mainly follows a power-law with the spectral index $\gamma \sim 3$. Therefore, the flux Φ_ν is multiplied by E^3 for better comparison. The plots are averaged from $\cos\theta_z = 0.0$ till $\cos\theta_z = 0.1$ (left) and from $\cos\theta_z = 0.9$ till $\cos\theta_z = 1.0$ (right), respectively.

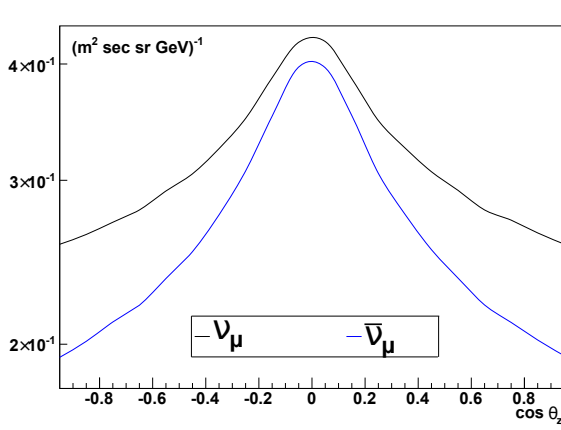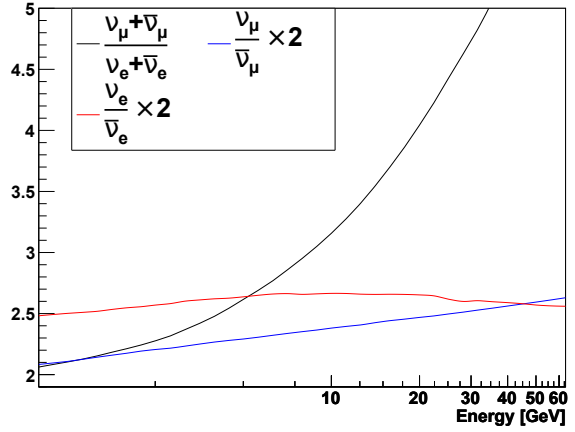Figure 4.2: Flux at $10\,\text{GeV}$: zenith angle slope of muon neutrinos and antineutrinos, respectively.

Figure 4.3: Theoretical neutrino Flux ratios of Eq. 2.2: these ratios are essentially independent of the primary cosmic ray spectrum. Details of the calculation in [30].
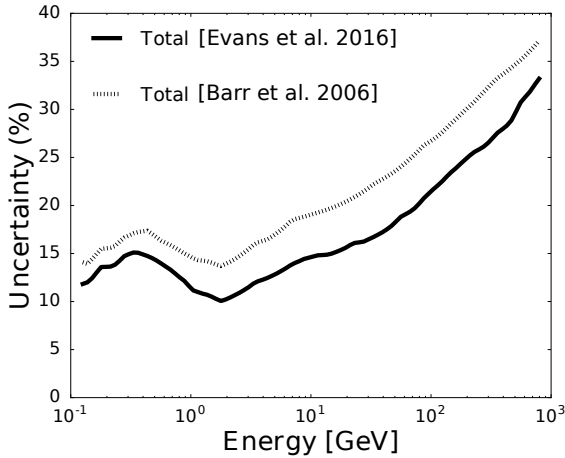
Figure 4.4: Flux uncertainties for muon neutrinos plotted as a function of neutrino energy. Calculation of the Bartol-Group 2006 [34] compared to a revaluation by [35]. The uncertainties dropped during the the last decade due to better measurements. Adopted from [35].
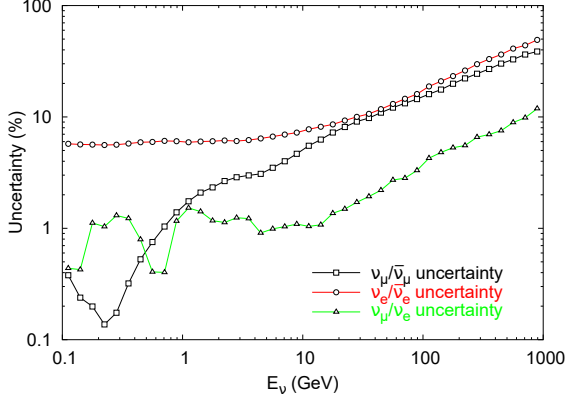
Figure 4.5: Uncertainties in neutrino-type ratios as a function of neutrino energy. $\nu_\mu/\overline{\nu}_\mu$ is shown with (black) lines with squares, $\nu_e/\overline{\nu}_e$ with (red) lines with circles and $(\nu_\mu + \overline{\nu}_\mu)/(\nu_e + \overline{\nu}_e)$ with (green) lines with triangles. Taken from [34].
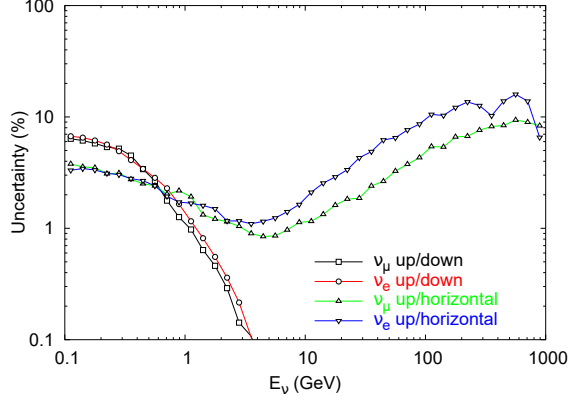
Figure 4.6: Uncertainties in directional ratios as a function of neutrino energy. 'up' is defined as $\cos\theta_z < -0.6$, 'down' as $\cos\theta_z > 0.6$ and horizontal as $|\cos\theta_z| < 0.3$. Taken from [34].

4.2 Calculation of the detector response

To estimate the measured rates using the initial fluxes, the following steps have to be made: first the differential neutrino flux has to be convoluted with the cross-section and effective mass to get a rate per E-$\cos\theta_z$-bin for each flavour. Then the reconstructed energy and zenith angle have to be estimated via a binwise smearing. Binwise smearing means that for each E-$\cos\theta_z$-bin a E-$\cos\theta_z$-histogram, which shows how the bin is smeared, is calculated. Therefore, the interaction kinematics as well as the limited detector resolution have to be taken into account. Finally the rates of all neutrino flavours have to be added up as no flavour identification is assumed.

4.2.1 Rates

The rate density for a specific neutrino type α is given by:

$$\frac{dn_\alpha(E, \cos\theta_z)}{dE\, d\cos\theta_z\, dt} = \frac{18 N_A}{m_{\text{mol}}} \cdot 2\pi \Phi_\alpha(E, \cos\theta_z) \cdot \sigma^\alpha(E) \cdot \rho V_{\text{eff}, \alpha}, \tag{4.1}$$

with differential neutrino flux Φ_α (from [25] azimuth averaged at solar minimum), the cross-section per nucleon σ^α and the effective detector mass $\rho V_{\text{eff}, \alpha}$ as obtained previously (Sec. 3.4.2). $18 \cdot N_A = m_{\text{mol}}$ is the number of target particles per unit mass and for water the molar mass is $m_{\text{mol}} = 18\,\text{g/mol}$.

For the CC cross-sections a parametrization of [36] by [37] is taken (see Eq. 4.2 for $E > 3\,\text{GeV}$) and the NC cross-sections are taken to be 1/3 of the CC cross-sections [38].

$$\frac{\sigma_{CC}^\nu}{E} = \left(-0.063 \log\left(\frac{E}{\text{GeV}}\right) + 0.804\right) \times 10^{-42}\,\text{m}^2\,\text{GeV}^{-1}, \tag{4.2}$$

$$\frac{\sigma_{CC}^{\overline{\nu}}}{E} = \left(-0.022 \log\left(\frac{E}{\text{GeV}}\right) + 0.372\right) \times 10^{-42}\,\text{m}^2\,\text{GeV}^{-1}$$

4.2.2 Kinematic smearing

The Bjorken inelasticity parameter $y = \frac{E - E_l}{E}$, with the energy E_l of the outgoing lepton, describes the fraction of the energy transferred to the hadronic cascade due to the kinematics of the interaction. For CC events it is assumed that the lepton energy as well as the energy of hadronic cascade can be measured such that the neutrino energy can be deduced, whereas the reconstructed direction is given by the direction of the outgoing lepton. To account for the deviation between the lepton and the neutrino direction, the neutrino direction has to be smeared according to the Bjorken y distribution. (It is to some extend possible to deduce the direction from the lepton as well as the direction from the hadron shower. Thus, this smearing step tends to underestimate the directional resolution, i.e. it is more strongly smeared than it should be.) For NC events the energy and direction of the outgoing neutrino is unavailable and only the direction and energy of the hadronic cascade can be measured. Such that the direction as well as the energy has to be smeared and the correlation between both smearings has to be considered.

The space angle γ between the incoming neutrino and the outgoing lepton or cascade can be calculated in the following way:

$$\cos \gamma = \sin \theta_{\mathrm{in}} \sin \theta_{\mathrm{out}} \cdot \cos \Delta\varphi + \cos \theta_{\mathrm{in}} \cos \theta_{\mathrm{out}}, \tag{4.3}$$

whereby θ_{in} is the zenith angle of the incoming neutrino, θ_{out} the zenith angle of outgoing particle, and $\Delta\varphi$ the difference in the horizontal angle.

The mean Bjorken y is nearly constant above a few GeV and is higher for neutrinos than for anti-neutrinos (see Fig. 4.7). This means that the space angle for anti-neutrino CC events is smaller on the average than for neutrinos and greater for NC events, respectively.
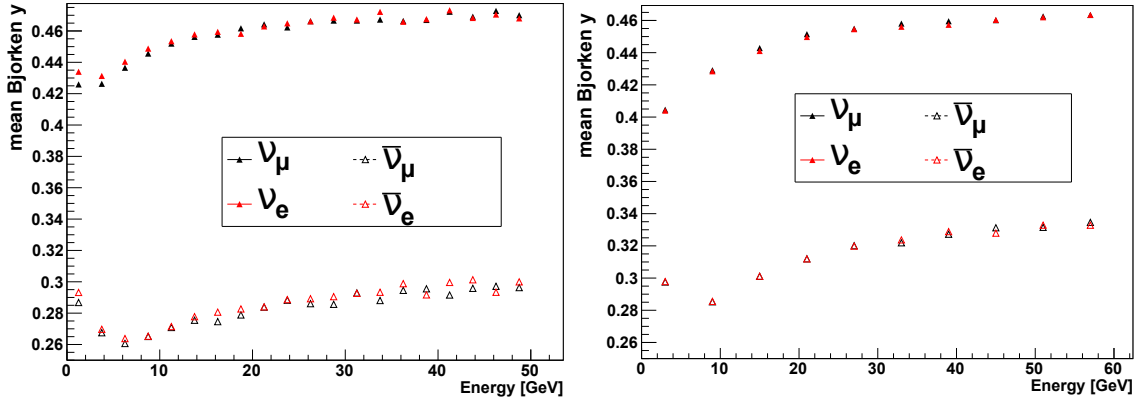

Figure 4.7: Mean Bjorken y - left: CC, right: NC - nearly constant above a few GeV and higher for neutrinos than for anti-neutrinos. The MC-simulation described in Sec. 2.6 was used.

Charged current (CC) events

Parametrization of the space angle distribution is done via a fitted Landau distribution in energy bins analogue to [37]. Two parameters describing the Landau distribution are the most probable value (MPV) and the spread ω. A relation between both parameters (Eq. 4.4) and between ω and E can be deduced (Eq. 4.5,Fig. 4.8).
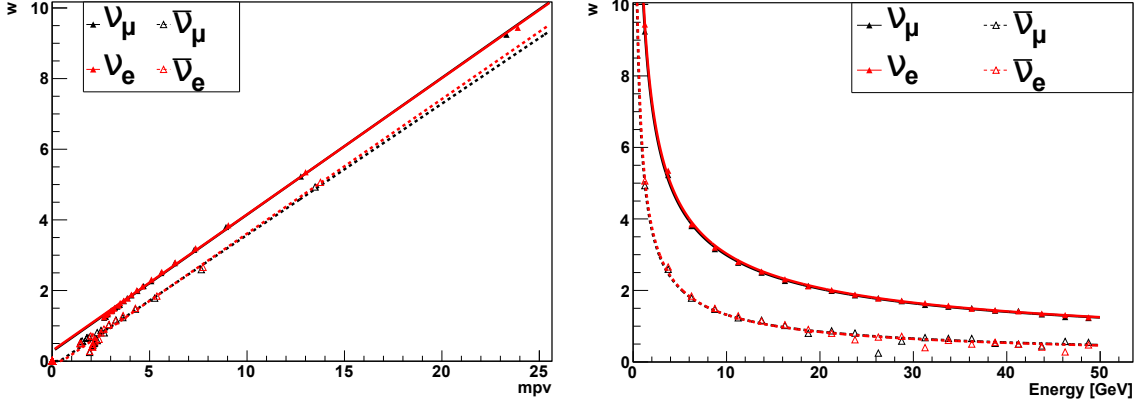
Figure 4.8: Kinematics CC - left: relation between MPV and ω, right: relation between ω and E. The MC-simulation described in Sec. 2.6 was used.

$$\omega_{\nu_\mu} = 0.39 \cdot \mathrm{MPV}_{\nu_\mu} + 0.27 \qquad\qquad \omega_{\nu_e} = 0.39 \cdot \mathrm{MPV}_{\nu_e} + 0.30 \qquad (4.4)$$
$$\omega_{\bar{\nu}_\mu} = 0.37 \cdot \mathrm{MPV}_{\bar{\nu}_\mu} - 0.14 \qquad\qquad \omega_{\bar{\nu}_e} = 0.38 \cdot \mathrm{MPV}_{\bar{\nu}_\mu} - 0.20$$

$$\omega_{\nu_\mu} = 10.8 \left(\frac{m_p}{E}\right)^{0.55} \qquad\qquad \omega_{\nu_e} = 11.1 \left(\frac{m_p}{E}\right)^{0.55} \qquad (4.5)$$
$$\omega_{\bar{\nu}_\mu} = 6.0 \left(\frac{m_p}{E}\right)^{0.64} \qquad\qquad \omega_{\bar{\nu}_e} = 6.2 \left(\frac{m_p}{E}\right)^{0.65}$$

Therefore, the obtained Landau distribution $L(\gamma, E)$ is a function only dependent on space angle $\gamma(\theta_{z,\mathrm{in}}, \theta_{z,out}, \varphi)$ and energy E. The fraction of the rate in a E-$\cos\theta_{z,in}$-bin ending up in E-$\cos\theta_{z,out}$-bin can then be calculated by an integral over the $\cos\theta_z$-bin-edges and φ:

$$N(E, \theta_{z,\mathrm{in}}, \theta_{z,\mathrm{out}}) = \int_{\theta_{z,\mathrm{out,low\ edge}}}^{\theta_{z,\mathrm{out,upper\ edge}}} \int_0^{2\pi} \frac{L(\gamma, E)}{2\pi \sin\gamma} \sin\theta_z d\theta_z d\varphi. \qquad (4.6)$$

The factor $2\pi \sin\gamma$ is a phase space correction, which accounts for more possibilities to obtain a larger value of γ.

Neutral current (NC) events

For NC events no such parametrization was found. Therefore, a space angle distribution in energy and Bjorken y slices is obtained from MC-simulation (Sec. 2.6) and smoothed in order to account for limited statistics. The bins of the obtained three dimensional histogram serve as sampling points for interpolation of points in this 3D space. A similar approach to the one described above is chosen: for every bin in the E-$\cos\theta_z$-histogram a E-$\cos\theta_z$-histogram for smearing is calculated.

Then it is looped over every E-$\cos\theta_z$-bin in each E-$\cos\theta_z$-smearing-histogram. It is integrated over the bin boundaries and for each energy value the corresponding Bjorken y is calculated. Then it is integrated over the resulting $\theta_{z,\mathrm{out}}$-φ_{out} -combinations to obtain the space angle γ. The value of the energy-y-γ-coordinates is interpolated from the 3D-histogram.
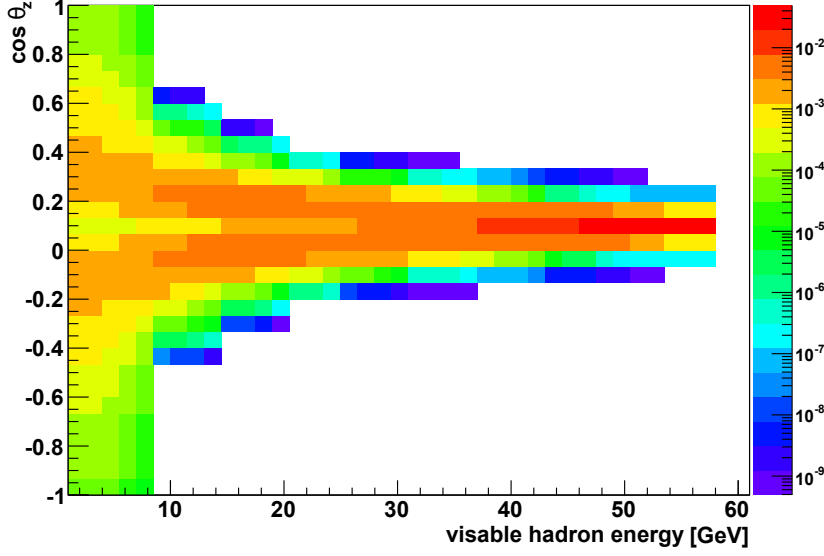
Figure 4.9: Kinematic smearing NC example: correlation between smearing in energy and zenith angle. Initial values: $E_\nu = 57.25\,\mathrm{GeV}$ and $\cos\theta_z = 0.10$. The histogram is normalised such that it's integral is 1.

One of the resulting $E\text{-}\cos\theta_z$-smearing-histograms is seen in Fig. 4.9. The initial energy and zenith angle of this histogram are $E_\nu = 57.25\,\mathrm{GeV}$ and $\cos\theta_z = 0.10$, respectively. The less energy is transferred to the hadron, the wider is the zenith angle distribution due to relativistic boosting.

4.2.3 Detector resolution smearing

In the second smearing step the limited detector resolution is taken into account analogue to [37]. The detector resolution in space angle σ_γ and energy σ_E is taken from [39]. As only values in the interval $1\,\mathrm{GeV}$ to $20\,\mathrm{GeV}$ are provided, the energy dependency was parametrized by power-laws to extrapolate to higher energies (see Fig. 4.10).
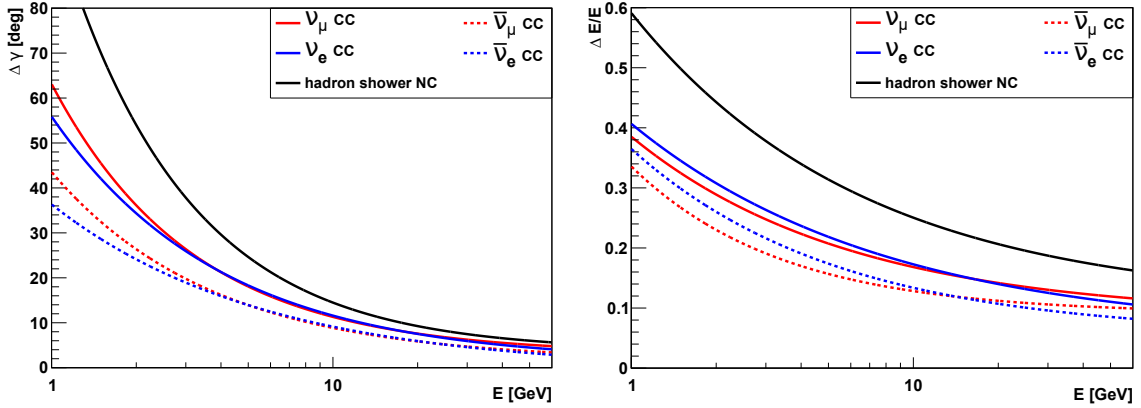
Figure 4.10: Parametrization of energy dependent detector resolution in space angle (left) and energy (right). For CC-interactions the achievable resolution of muon and electron (anti-)neutrino events is plotted. For NC-interactions the achievable resolution of hadron showers is plotted.

Furthermore a systematic shift in energy for NC events is used to account for the lower light yield of hadron showers [39]:

$$f_h(E_h) = 1 - 0.681 \left(\frac{E_h}{0.863} \right)^{-0.207}. \tag{4.7}$$

The detector resolution can be approximately implemented by a two dimensional Gaussian smearing in energy and space angle, whereby the Gaussian in each dimension is given by:

$$G(x, x_0, \sigma_x) = \frac{1}{\mathcal{N}} \exp \left(-\frac{(x - x_0)^2}{2\sigma_x^2} \right), \quad x = E, \gamma. \tag{4.8}$$

For each initial bin in the E-$\cos\theta_z$-plane with the bin centre coordinates (E_k, θ_l) a smearing histogram is calculated. The bin centre coordinates in the smearing histogram are referred to as (E_i, θ_j). The content of bin (i,j) in the smeared histogram for the initial bin (k,l) is then given by:

$$N_{ij}^{kl} = \int_{E_{i,\mathrm{low}}}^{E_{i,\mathrm{up}}} dE_i \int_{\theta_{j,\mathrm{low}}}^{\theta_{j,\mathrm{up}}} \sin\theta_j d\theta_j \int_0^{2\pi} d\varphi \, G(E_i, E_k, \sigma_E(E_k)) \cdot G(\gamma_{jl}, \gamma_{ll}, \sigma_\gamma(E_k)), \tag{4.9}$$

whereby the subscripts 'low' and 'up' denote the lower and upper bin edges. In this notation the space angle γ (Eq. 4.3) can be expressed as:

$$\cos\gamma_{jl} = \sin\theta_j \sin\theta_l \cdot \cos\varphi + \cos\theta_j \cos\theta_l. \tag{4.10}$$

Finally each smearing histogram is normalized to the content of its corresponding bin (k,l) in the initial histogram.

4.3 Flux variations

The HKKM15 [25] neutrino flux is varied in different ways to investigate to which extent the flux uncertainties (see Sec. 4.1) can be reduced by using the downgoing neutrino flux. Beside these flux uncertainties even a possible shift in the detector energy response is examined.

The variations are applied to the neutrino flux in a toy parametrized way. For a more sophisticated study, variations should be applied to the primaries and interactions as the Bartol-Group did [34]. The difference could mainly lead to an incorrect handling of correlations between the variations.

The normal and varied E-$\cos\theta_z$-rate-histograms are calculated in the energy range from $1\,\mathrm{GeV}$ to $91\,\mathrm{GeV}$ and in the full zenith range $-1 < \cos\theta_z < 1$. To restrict the analysis to the downgoing phase space region without turnon effects and sufficient flux, only bins with $10 < E < 61\,\mathrm{GeV}$ and $\cos\theta_z > 0$ are selected after application of smearing and variation. The larger initial ranges are taken to account for smearing and shifting (caused by variations) effects, through which bins out of the selected range affect bins in the selected range. In that way, for example, upgoing events that were reconstructed as downgoing are included and smearing and shifting of energy is considered.

After this range restriction E-$\cos\theta_z$-rate-histograms with varied flux are compared to the one without variation. Therefore, an asymmetry variable is defined to identify the phase space regions where the flux variation effects are largest:

$$\mathcal{A}_i = \frac{R_{\mathrm{var},i} - R_i}{\sqrt{R_i}}, \tag{4.11}$$

with R_i =normal rate in bin i and $R_{var,i}$ =varied rate in bin i.

Similar to the significance estimation approach for measuring the mass hierarchy of [12], the squared significance after one year can be estimated as:

$$\mathcal{S}^2 = \sum_i^{\mathrm{NBins}} \mathcal{A}_i^2 = \sum_i^{\mathrm{NBins}} \frac{(R_{\mathrm{var},i} - R_i)^2}{R_i}. \tag{4.12}$$

Each of the variations can have similar effects on the rate, thus, it is important to see how well it can be differentiated between them. Therefore, two variations were applied simultaneously. In that way 2D significance plots, which show the discrimination power between the variated rate and the standard rate, were created for each parameter combination. For a more sophisticated study of correlations a N-dim minimization fit should be carried out. But for time limitations this study is restricted to a two dimensional approach.

In the following subsections the asymmetries induced by variations and the correlations between them are discussed. Thereby two kinds of plots are used:

- asymmetry plots: on the x-axis the reconstructed (smeared) energy and on the y-axis the reconstructed $\cos\theta_z$ is plotted. The asymmetry is colour coded (example: Fig. 4.11). The significance in σ and the variation of the parameter under question in percent are given for each plot.

- correlation plots: on each axis (x- and y-axis) the variation of one parameter is given in %. The significance of discriminating this variation from the unvaried case is colour coded. Furthermore, the $1\,\sigma$ and $3\,\sigma$ isolines are shown. The parameter range is chosen so that the correlation is well visible. Therefore, the range is mostly chosen as 3 times the obtained reachable uncertainty without correlation, unless 3 times the current uncertainty is lower than this value (example: Fig. 4.17).

4.3.1 Variations affecting normalisation

Flux: overall normalization The main uncertainty is the overall flux normalization of the neutrino flux that is about $15\,\%$. It is implemented in a way that the flux of each flavour is scaled by the same factor resulting in an overall increase/decrease of the rate. The induced asymmetry mainly looks like the rate spectrum (see Fig. 4.11) and is similar to Fig. 4.12.

Detector: energy scale The energy scale is a linear scaling in energy accounting for a misreconstruction in energy (uncertainty in PMT efficiency and optical water properties). Its uncertainty is assumed to be about $10\,\%$. As it is a detector intrinsic factor, the offset is applied after the kinematic smearing. It is implemented in a way that shifts by $a \cdot E$ to the right: $E' = E \cdot (1 + a)$.
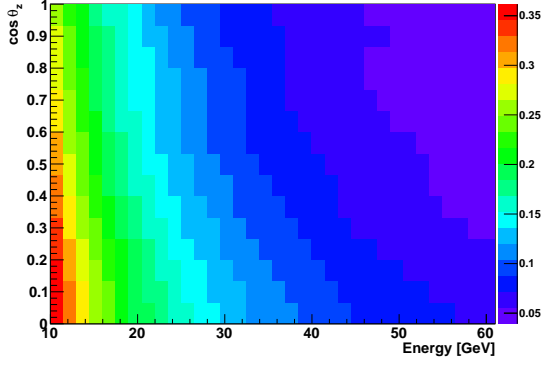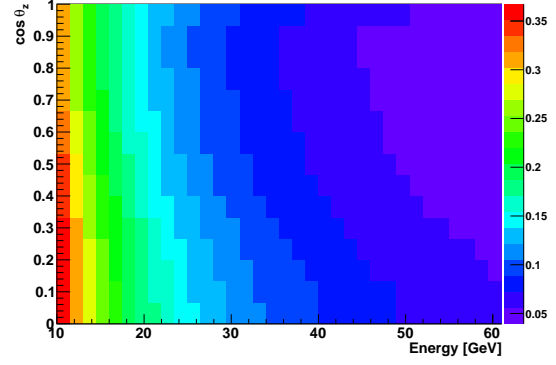
Figure 4.11: Asymmetry: flux normalization $(3\,\sigma,\ 3.3\,\%)$.

Figure 4.12: Asymmetry: energy scale $(3\,\sigma,\ 1.4\,\%)$.

Correlation A rough approximation shows that a variation of the energy scale translates into a variation of the flux normalization (N):

$$R = \Phi\sigma \sim N \cdot E^{-2} \rightarrow R' = N \cdot ((1+a) \cdot E)^{-2} = \frac{1}{(1+a)^2} N \cdot E^{-2} = N' \cdot E^{-2}. \tag{4.13}$$

Therefore, the asymmetry induced by a positive energy scale mainly looks like the rate spectrum (see Fig. 4.12). This can also be seen in the correlation plot of energy scale and flux normalization (Fig. 4.13). The correlation is linear: the error on the flux normalization is about two times the error on the energy scale. Both are fully correlated within their uncertainty range. So to determine one of them better than known, the other one has to be independently determined by another method. On the other hand, the correlation effectively makes one parameter out of two. As both parameters are currently free parameters of the mass hierarchy fit [13], the number of free parameters could be lowered in this way.

The zenith dependency of the flux shape in energy (Fig. 4.1) induces a deviation of the rough approximation above. The obtained nearly full correlation already indicates that the discrimination strength due to this zenith dependency is low. To identify the magnitude of this discrimination strength, a variation of energy scale which was normalised to the total rate was investigated additionally (Fig. 4.14). One sigma is reached for a negative variation of $a = -11\,\%$ or a positive variation of $a = 22\,\%$.
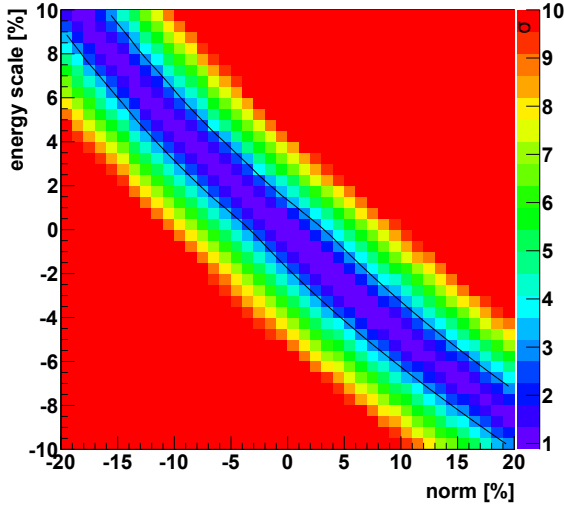
Figure 4.13: Correlation of norm and energy scale: strongly correlated - an energy scale shift to higher energies can be reversed by a lower flux normalization. The 1σ isoline is not shown, because of resolution issues.
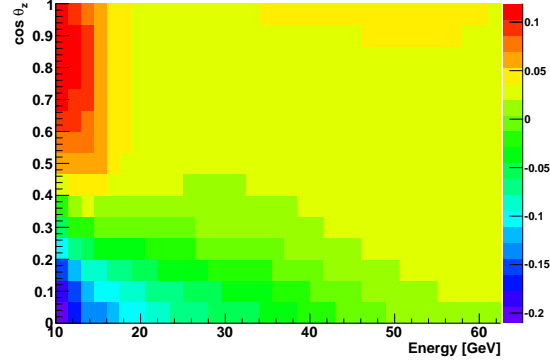
Figure 4.14: Asymmetry: energy scale normalised to overall rate (1σ, 22 %).

4.3.2 Variations affecting zenith slope

Flux: zenith slope Variations of atmospheric parameters like density and temperature would affect the probability of muons to decay towards the horizon. This would alter the slope in zenith angle of the neutrino flux.

Therefore, the flux is tested for a linear slope variation parametrized by:

$$\Phi' = \Phi \cdot (1 + 2a\cos\theta_z)\frac{\Phi_{\mathrm{norm}}}{\Phi'_{\mathrm{norm}}}, \tag{4.14}$$

whereby a is varied. The renormalization ($\Phi_{\mathrm{norm}}/\Phi'_{\mathrm{norm}}$) is chosen to investigate the zenith slope variation independently of the flux normalization. The prefactor 2 of a is taken such that a corresponds approximately to the percental variation of the downward to horizontal ratio. For example, in the case of $a = 10\,\%$ the percental variation of the downward to horizontal ratio goes from 9 % (at 10 GeV) to 11 % (at 60 GeV). The current uncertainty on this ratio is about 4 %.

The asymmetry originating from the variation of zenith slope (Fig. 4.15) looks different from most other asymmetries. A decrease at low $\cos\theta_z$ and an increase at high $\cos\theta_z$ is visible. This decrease/increase structure mainly originates from normalizing the histogram to the flux normalization before variation.

Detector: $\cos\theta_z$-dependent energy scale Apart from the normal energy scale (Sec. 4.3.1), also one with a $\cos\theta_z$-dependency was evaluated: $E' = E \cdot (1 + a\cos\theta_z)$. This dependency can occur due to the multi PMT structure of DOMs. As the DOMs get dirty in the upper part, it could be that high $\cos\theta_z$ values lead to less hits and therefore to a lower reconstructed energy. The definition of the energy scale with $\cos\theta_z$-dependency gives rise to an excess at high $\cos\theta_z$, but it

was normalised to the total rate to compare it to the $\cos\theta_z$ flux slope (see Fig. 4.16). Following the introduction of the $\cos\theta_z$-dependency, a negative sign of the variation is more likely. The current uncertainty is estimated to have about the same value as the uncertainty on the normal energy scale: 10 %.
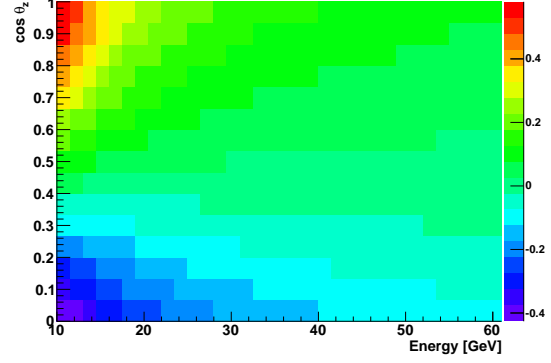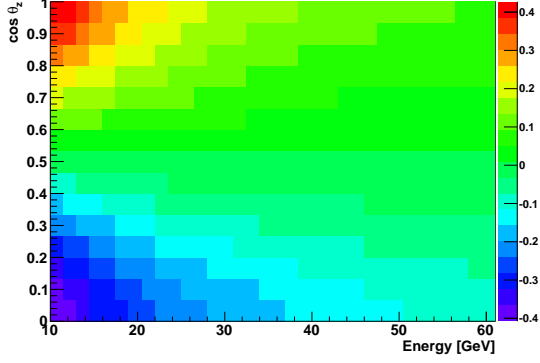
Figure 4.15: Asymmetry: zenith slope ($3\,\sigma$, 7.3 %).

Figure 4.16: Asymmetry: energy scale with $\cos\theta_z$-dependency ($3\,\sigma$, 5 %).

Correlation The zenith slope and $\cos\theta_z$-dependent energy scale are weakly correlated, as they both influence the zenith dependency (see Fig. 4.17). It would be advisable to determine the $\cos\theta_z$-dependent energy scale independently by using event by event calibration methods. On the other hand the uncertainty on $\cos\theta_z$-dependent energy scale could be lowered, as the zenith slope is relatively well known.
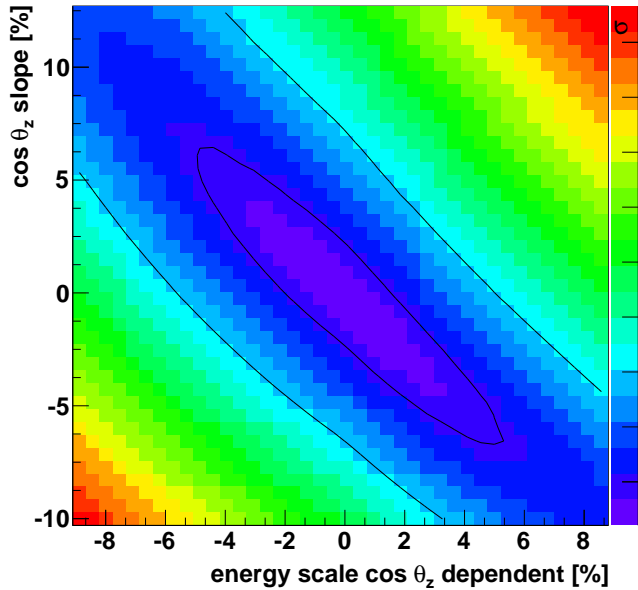
Figure 4.17: Correlation of zenith slope and $\cos\theta_z$-dependent energy scale with normalization: weakly correlated, as they induce similar asymmetries.

4.3.3 Flavour and antimatter ratios

The variation of the three ratios (2.2) are examined: The ratio of muon neutrinos ν_μ to electron neutrinos ν_e and the ratios between neutrinos $\nu_{\mu,e}$ and antineutrinos $\overline{\nu}_{\mu,e}$.

Each is implemented in a way that the ratio under question is scaled by a factor a, leaving the total flux and the other ratios invariant. This means, by varying the flavour ratio $\frac{\Phi'_{\nu_\mu+\overline{\nu}_\mu}}{\Phi'_{\nu_e+\overline{\nu}_e}} = a \cdot \frac{\Phi_{\nu_\mu+\overline{\nu}_\mu}}{\Phi_{\nu_e+\overline{\nu}_e}}$ the norm $\Phi_{tot} = \Phi_{\nu_\mu+\overline{\nu}_\mu} + \Phi_{\nu_e+\overline{\nu}_e} \overset{!}{=} \Phi'_{tot}$ as well as the antimatter ratios $\frac{\Phi_\nu}{\Phi_{\overline{\nu}}} \overset{!}{=} \frac{\Phi'_\nu}{\Phi'_{\overline{\nu}}}$ should be left invariant. This results in following formulas:

$$\Phi'_{\nu_\mu+\overline{\nu}_\mu} = \frac{a \cdot \Phi_{\nu_\mu+\overline{\nu}_\mu} \cdot \Phi_{tot}}{\Phi_{\nu_e+\overline{\nu}_e} + a \cdot \Phi_{\nu_\mu+\overline{\nu}_\mu}}, \qquad \Phi'_{\nu_e+\overline{\nu}_e} = \frac{\Phi_{\nu_e+\overline{\nu}_e} \cdot \Phi_{tot}}{\Phi_{\nu_e+\overline{\nu}_e} + a \cdot \Phi_{\nu_\mu+\overline{\nu}_\mu}}, \qquad (4.15)$$

$$\Phi'_{\nu_\mu} = \Phi'_{\nu_\mu+\overline{\nu}_\mu}/(1 + \frac{\Phi_{\overline{\nu}_\mu}}{\Phi_{\nu_\mu}}), \qquad \Phi'_{\nu_e} = \Phi'_{\nu_e+\overline{\nu}_e}/(1 + \frac{\Phi_{\overline{\nu}_e}}{\Phi_{\nu_e}}), \qquad (4.16)$$

$$\Phi'_{\overline{\nu}_\mu} = \Phi'_{\nu_\mu+\overline{\nu}_\mu}/(1 + \frac{\Phi_{\nu_\mu}}{\Phi_{\overline{\nu}_\mu}}), \qquad \Phi'_{\overline{\nu}_e} = \Phi'_{\nu_e+\overline{\nu}_e}/(1 + \frac{\Phi_{\nu_e}}{\Phi_{\overline{\nu}_e}}). \qquad (4.17)$$

The antimatter ratios are handled for each flavour separately:

$$\Phi'_{\overline{\nu}_\mu} = (\Phi'_{\nu_\mu+\overline{\nu}_\mu}/(1 + a \cdot \frac{\Phi_{\nu_\mu}}{\Phi_{\overline{\nu}_\mu}})), \qquad \Phi'_{\nu_\mu} = a \cdot \frac{\Phi_{\nu_\mu}}{\Phi_{\overline{\nu}_\mu}} \cdot \Phi'_{\overline{\nu}_e}, \qquad (4.18)$$

$$\Phi'_{\overline{\nu}_e} = (\Phi'_{\nu_e+\overline{\nu}_e}/(1 + a \cdot \frac{\Phi_{\nu_e}}{\Phi_{\overline{\nu}_e}})), \qquad \Phi'_{\nu_e} = a \cdot \frac{\Phi_{\nu_e}}{\Phi_{\overline{\nu}_e}} \cdot \Phi'_{\overline{\nu}_e}. \qquad (4.19)$$

As no flavour identification is assumed, only the zenith dependency of the ratios and the different cross-sections for matter and antimatter leave a possibility of identification. A greater $(\nu_\mu + \overline{\nu}_\mu)/(\nu_e + \overline{\nu}_e)$ ratio results in an excess at the zenith but even a greater $\nu_\mu/\overline{\nu}_\mu$ ratio results in a weak excess at the zenith (see Sec. 4.1 and Fig. 4.18). The correlation between both is seen in Fig. 4.19. However, a variation in the $\nu_e/\overline{\nu}_e$ ratio in the allowed regime leads to no identifiable pattern. The theoretical errors on each ratio are much lower than what could be achieved within one year without flavour identification.

Fig. 4.20 shows the correlation between $\nu_\mu/\overline{\nu}_\mu$ ratio and flux normalization. Both are strongly correlated mainly due to the different cross-sections of neutrinos and antineutrinos. (The cross-section is fully correlated to the flux normalization as $R = \sigma\Phi$.)

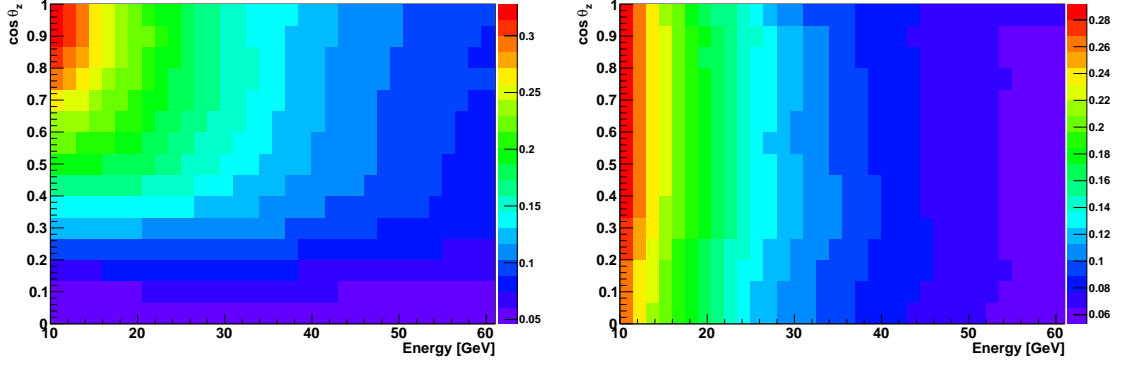For a tabular overview of uncertainties on the variations and further correlation plots see Appendix C.

Figure 4.18: Asymmetry: $(\nu_\mu + \overline{\nu}_\mu)/(\nu_e + \overline{\nu}_e)$ ratio (left) $(3\,\sigma,\ 35\,\%)$ and $\nu_\mu/\overline{\nu}_\mu$ ratio (right) $(3\,\sigma,\ 22\,\%)$.
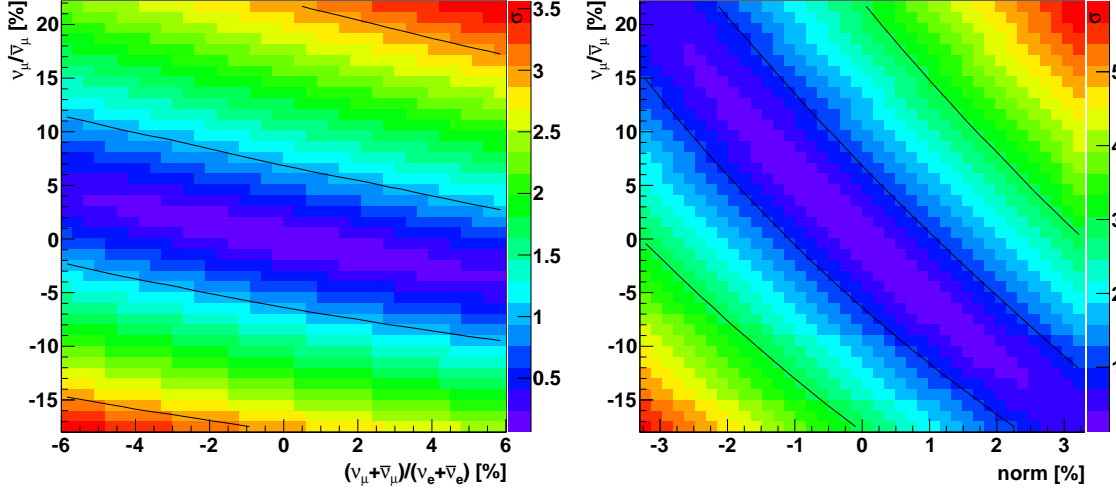

Figure 4.19: Correlation of $\nu_\mu/\overline{\nu}_\mu$ ratio and $(\nu_\mu + \overline{\nu}_\mu)/(\nu_e + \overline{\nu}_e)$ ratio: correlated, but as $(\nu_\mu + \overline{\nu}_\mu)/(\nu_e + \overline{\nu}_e)$ is already well known, it is negligible.
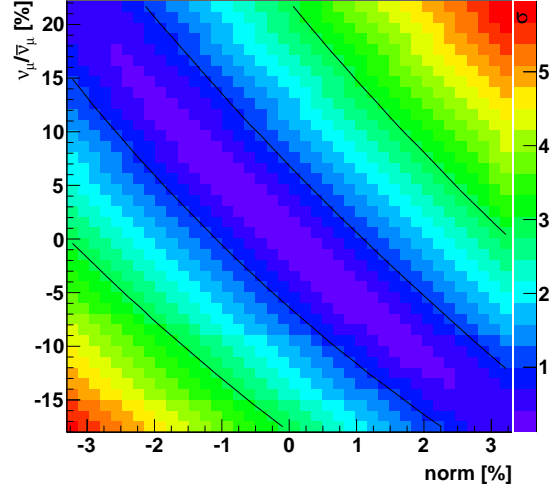
Figure 4.20: Correlation of $\nu_\mu/\overline{\nu}_\mu$ ratio and flux normalization: strongly correlated mainly due to the different cross-sections of neutrinos and antineutrinos. (The cross-section is fully correlated to the flux normalization as $R = \sigma\Phi$.)

4.3.4 Conclusion

The energy and zenith angle dependent interaction rate was calculated by using the HKKM15 flux, the cross-section and the effective mass, which was obtained in the previous chapter. How the energy and zenith angle would be reconstructed, the so called 'detector response', is estimated by a smearing procedure. Several variations in the flux and the interaction rate were applied in order to investigate to which precision flux (normalization, zenith slope, flavour ratios) and detector response (energy scale) parameters can be determined by using the downgoing neutrino flux. The flux normalization is fully correlated with the energy scale within their current uncertainties. Hence, one of both has to be independently determined to obtain a lower uncertainty on the other one. On the other hand, the correlation makes effectively one parameter out of two. As both parameters are currently free parameters of the mass hierarchy fit [13], the number of free parameters could be lowered in this way. As the zenith slope is already relatively well known, it cannot significantly better be determined by a measurement of the downgoing neutrino flux with ORCA. The flavour ratios are not able to be determined without flavour identification (for simplicity no flavour identification was assumed here).

Note that the effective mass is obtained and applied for a 6 m vertical spaced detector whereas the actual detector will be 9 m vertical spaced. The effective mass is expected to scale with the detector. This will reduce the uncertainties on the parameters.

Chapter 5

Conclusion and Outlook

One of the still unknown parameters of neutrino oscillation is the sign of the largest mass difference, called neutrino mass hierarchy (NMH). This sign can be determined via oscillations in matter. The KM3NeT-Collaboration builds the Cherenkov detector ORCA in the Mediterranean deep sea to use atmospheric neutrino traversing the Earth for probing the NMH.

A crucial systematic for the neutrino mass hierarchy measurement is the neutrino flux normalization. Therefore, an independent flux measurement of downgoing neutrinos is intended. However, the many orders of magnitude greater rate of atmospheric muons complicates this unoscillated neutrino flux measurement.

Accordingly, a muon veto was developed in this thesis. It uses a kind of fiducializing as it is used in similar detectors, i.e. the pattern of the first hits of an event gives information about whether the event started inside a fiducial volume or not. At first, a very clean hit selection was developed to be confident that the selected hits, from which information is deduced, are not just noise hits. Then, various parameters describing the pattern of the first hits are calculated and cuts are applied. Events, from which no reliable information can be deduced, are identified and rejected. By these criteria already a remaining contamination of atmospheric muons of less than $15\,\%$ can be achieved. Finally, a full reconstruction is applied and cuts on calculated parameters are placed. This decreases the contamination further down to about $1\,\%$. The effective mass for neutrinos after the muon veto is roughly $1.75\,\mathrm{Mton}$ for the neutrino energy regime above $10\,\mathrm{GeV}$, which corresponds to about nearly $50\,\%$ of the instrumented volume.

As the veto relies on the hit selections mentioned above, studies should be conducted on how well they perform if the noise rate is higher than simulated, for example because of bioluminescence. Maybe some of the hit selection parameters should be adjusted in that case. Moreover, the chosen veto configuration can still be optimized, for example, by relying more on the reconstruction methods.

Furthermore, assuming the detection of downward-going neutrinos with the obtained effective mass, an investigation was conducted on the achievable precision with which the atmospheric neutrino flux parameters can be determined within one year. The main problem is the full correlation between flux normalization and energy scale, which is a linear scaling in energy accounting for a energy uncertainty in the detector response. Therefore, only in combination with other calibration methods it will be possible to separate detector response parameters from flux parameters to

reduce the uncertainties on either of the both.

Unfortunately, the muon veto could only be conducted for a 6 m vertical spaced detector, whereas the final decision for the vertical spacing was 9 m. Therefore, some hit selection and veto parameters have to be scaled to adapt to the larger detector. If a similar good neutrino efficiency can be achieved, the effective mass will increase with the larger detector volume, i.e. the flux measurement will be more accurate.

In addition, it would be interesting to apply this veto strategy to the far more larger ARCA-detector. In this way astrophysical downgoing neutrinos could be detected.

Appendix A

Discarded rejection criteria

Finding good rejection criteria like in Sec. 3.3 was not a straight forward development. The presented criteria were altered in different ways before they reached their final configuration. But it was not just their configuration that was investigated, there were ideas to some other criteria, too. Those other criteria, which were discarded, are presented in this appendix.

Inner-criterion: L1 hits in fiducial volume and within time margin

The *Inner*-criterion was meant as a positive criterion for neutrinos: if there are hits in the inner part of the detector within the first nanoseconds, the particle was produced inside the detector. The disadvantage of this criterion is that it cannot exclude high energetic muons which go to centre of the detector on the shortest way and therefore produce hits in the inner part within the time margin. Nevertheless, these hits are mostly excludable with the *Outer*-criterion. This criterion can give no information about the event, if there is not the required number of hits within the time margin in the whole detector. In this case the criterion is labelled to have a bad accuracy and the criterion does not let the event pass. Low energetic neutrinos often get the bad accuracy label, therefore a connection of criteria has to have a logical OR between *Inner*-criterion and *Inner*-criterion with bad accuracy. As this criterion does not give any new information compared to the other criterions, it was finally dropped.

MeanDirTx-criterion: mean direction of hits without time margin

In some cases the hit selection does not work well and the first hits within the time margins of various criterions are just noise. Sometimes those events cannot even be characterized by the N_{hits}-rejection-part. Those are mainly events with muons flying radially inwards. For these cases a criterion similar to the *MeanDir*-criterion (see Sec. 3.3.1) was investigated that has no time margin: *MeanDirTx*-criterion. This is only a criterion on the mean direction of PMT hits located in the **mantel** (see Fig. 3.11).
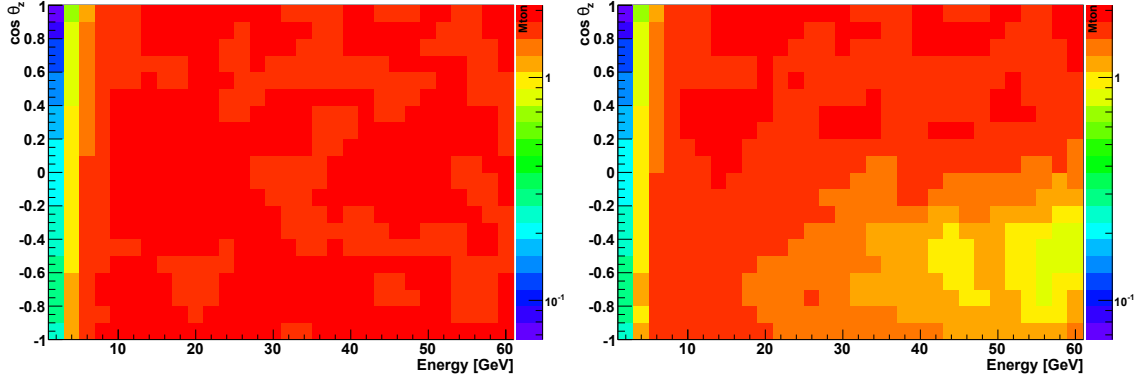
Figure A.1: Effective mass distortion of *MeanDirTx*-criterion: *Connect*-criterion without *MeanDirTx*-criterion (left) shows no zenith angle dependency. Whereas additionally applying *MeanDirTx*-criterion causes a deficit of upgoing neutrinos (right).

If the standard deviation of those PMT hits is lower than 0.4 and there are 5 or more PMT hits in the mantel, the following requirement is set: the mean cosine of angle between the PMT hit direction ($\overrightarrow{\mathrm{PMT}}$) and the radial outward direction ($\hat{\mathrm{e}}_{\mathrm{r}}$) has to be lower than 0.4 ($\overrightarrow{\mathrm{PMT}} \cdot \hat{\mathrm{e}}_{\mathrm{r}} < 0.4 \rightarrow$ not pointing outwards) and the number of PMT hits in the **corner** has to be lower or equal 5. In that way only events with hits explicitly pointing outward should be rejected. But it was observed that such a criterion would be accompanied by a distortion of the neutrino effective mass E-$\cos\theta_z$-plane (see Fig. A.1 and Sec. 3.4.2). It is not sure why this is the case. But as most of the above described events can even be rejected by a cut on the reconstructed track starting point, further investigation on this criterion was regarded to be not worth the time.

Back projection of mean DOM direction

Another possibility of using the directional information of PMT hits was investigated as an alternative to the *MeanDir*-criterion. The idea is similar to the *MeanDir*-criterion (see Sec. 3.3.1) but instead of dividing the detector into parts (see Fig. 3.11), another approach is taken. An intersection between the linear extension of the mean direction of each L1 hit with the surface of a cylindrical fiducial volume is searched for. If a L1 hit can be back-projected in that way onto the surface of the fiducial volume, the L1 hit points inward. The fraction of L1 hits that can be back-projected, gives information whether an event has its origin within the fiducial volume or not. The main advantage over the *MeanDir*-criterion would be that even the direction of L1 hits in the 'corner' could be used. However, the main disadvantage is that there is no parameter for the variance of the directions. Thus it is difficult to estimate its reliability. The described disadvantage dominated in the executed tests. In order to get similar or even better results compared to *MeanDir*-criterion there would be more work to do.

Median position of L1 hits

Even an alternative to the *MeanPos*-criterion (see Sec. 3.3.1) was examined. Instead of taking the mean position of L1 hits and discarding outliers, the idea was to take the median position of L1 hits. However, the median position is not uniformly distributed like the mean position. The individual positions of DOMs were seen in the distribution instead. As this attempt offered no real advantage and had a more difficult distribution, it was not studied any further.
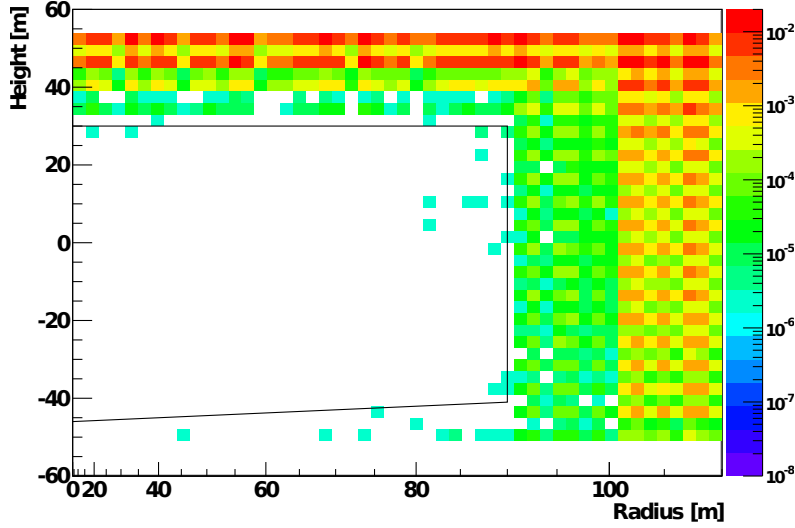
Figure A.2: Median position of luminous muon events. Similar to plot Fig. 3.12, but less uniformly distributed. Only 1.4 % of the muon events, which were used for Fig. 3.12, were used for this plot.

Appendix B

Combination of rejection criteria

This appendix belongs to the chosen connection between rejection criteria and the resulting contamination (see Sec. 3.4.1). Interesting questions are how strong each of the criteria is on its own and whether relying more on the reconstruction would result in a better neutrino efficiency. See Sec. 3.3.3 for explanation of the used nomenclature.

To recall: the reconstruction was executed if a weaker than normal cut on the mean position of hits (weak *MeanPos*-criterion) was passed. In that way it is possible to analyse at which point of the rejection criteria the reconstruction should set in. But it is not possible to analyse how the reconstruction would perform on its own. So in order to do a fair comparison lets set that at least the weak *MeanPos*-criterion has to be passed before comparing criteria. The weak *MeanPos*-criterion suppresses $\sim 99.5\,\%$ of the muon events and reaches a contamination of a bit less than ~ 200. Therefore, it saved a lot of calculation time to apply reconstruction only if the event passed this criterion without resulting in a big effect on the analysis. For all criteria in Fig. B.1 at least the weak *MeanPos*-criterion was passed.

It should be stressed again that each of the criteria has quite loose cuts and is designed in a way that they complement each other. This can especially be seen for criteria on the quality of the event like N_{hits}-rejection-part and fit quality. When they are applied on events that passed the weak *MeanPos*-criterion, these criteria seem to have a larger effect on neutrino efficiency than on the muon contamination (see Fig. B.1 left) and are therefore quite useless. Only by applying them after strong rejection criteria, it can be seen that criteria on the quality of the event exclude muon events that cannot be otherwise excluded (see Fig. 3.29). Furthermore, by only using the chosen cut on the reconstructed track starting point, the contamination is higher than using the *MeanPos*-criterion, as the track starting point was only used to exclude some remaining events in the chosen veto configuration (see Fig. B.1 left, *Reco part* stands for a logical AND between the reconstructed track starting point and fit quality).

Fig. B.1 (right) illustrates combinations of rejection criteria: a logical OR between *Outer*-criterion and *MeanDir*-criterion builds up the *Outer*-rejection-part, thereby gaining efficiency but worsen the contamination. Additionally, applying the N_{hits}-rejection-part lowers the contamination below the one reached by the *MeanPos*-rejection-part. The difference between *MeanPos*-criterion and *MeanPos*-rejection-part is only that *MeanPos*-rejection-part uses the error on the mean position additionally to the mean position.

To see how strong a cut on the reconstructed track starting point can be, a harder cut was chosen (see Fig. B.2). The new *Reco part* reaches a lower contamination and much better efficiency than the *Connect*-criterion. Fig. B.3 shows the performance of the rejection parts applied to events that passed the *Reco part* with the stronger cut. The AND connection between *Outer*-rejection-part and N_{hits}-rejection-part seems like a good deal. Thus, a 14 % higher effective mass could be reached by using: *weak MeanPos* AND *Outer part* AND N_{hit} *part* AND *(strong) Reco-part*. For this configuration the reconstruction sets in at a contamination of about 2. So depending on how much computational time is available, better configurations of the muon veto should be found. Even a boosted decision tree on the parameters calculated by the rejection criteria would help to find a better configuration.
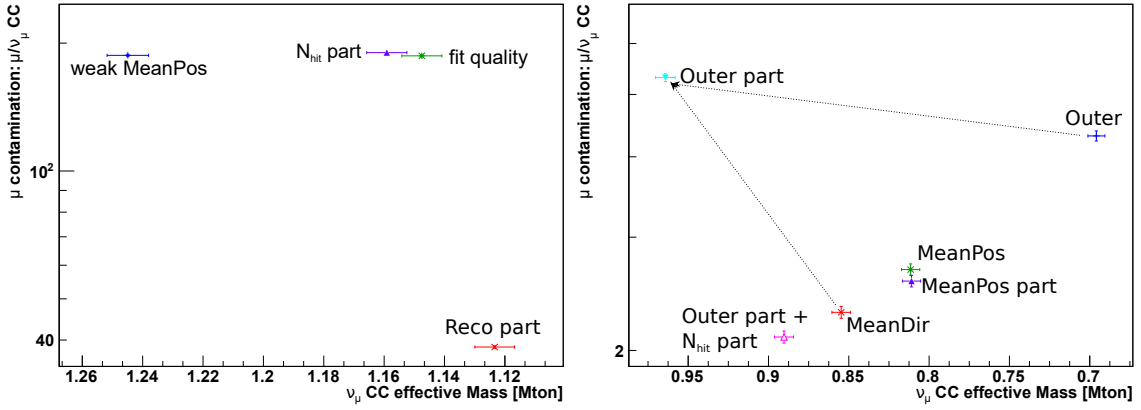
Figure B.1: Contamination vs effective mass averaged over energy and downgoing zenith angle range for ν_μ CC events. In both plots at least the weak *MeanPos*-criterion was passed. On the left, criteria that do not work on their own are shown. On the right, combinations of rejection criteria are illustrated.
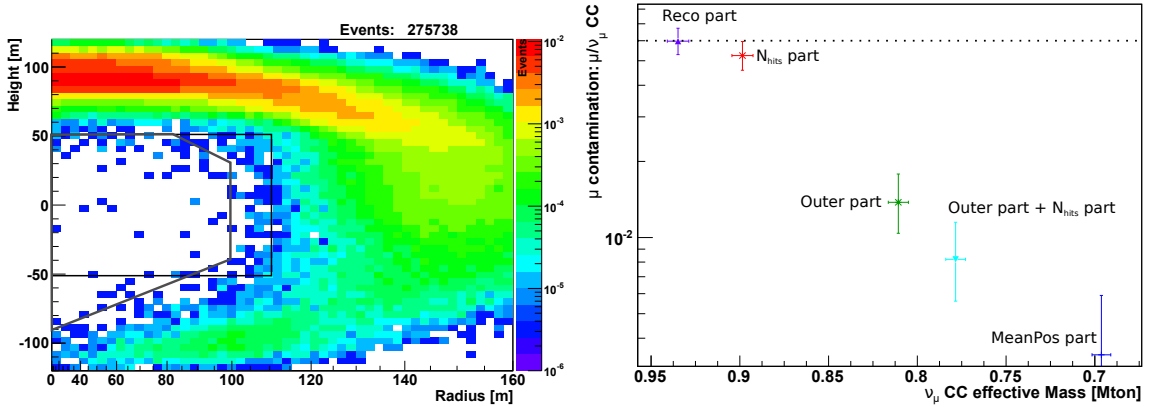
Figure B.2: Reconstructed track starting point of muon events passing weak *MeanPos*-criterion. New cut is shown in grey.

Figure B.3: Contamination vs effective mass averaged over energy and downgoing zenith angle range for ν_μ CC events. A stronger cut on the reconstructed track starting point was taken and the performance of the rejection parts applied to events that passed the *Reco part* is shown.

60

Appendix C

Further Flux investigations

This appendix belongs to the flux variation studies in Sec. 4.3.

Tab. C.1 gives an overview of the current uncertainties and within one year reachable uncertainties on the variations, whereby correlations are neglected. For example, the energy scale and flux normalization seem to be determinable to very good precision, but they are correlated. The normalised energy scale gives a better estimation how well the energy scale can be determined independently of the flux normalization. The (normalised) $\cos\theta_z$-dependent energy scale is correlated to the zenith slope and the not normalised $\cos\theta_z$-dependent energy scale is correlated to the normal energy scale. But even by neglecting correlations the flavour ratios are not able to be determined without flavour identification.

Some further correlations plots are presented here (Fig. C.1-Fig. C.16), too.

Table C.1: Percental uncertainties on flux parameters in the energy regime of $10-60\,\mathrm{GeV}$. Current uncertainties were evaluated by the Bartol-Group [34] and updated by [35] (see Sec. 4.1). Uncertainties at the significance levels $1\,\sigma$ and $3\,\sigma$ were obtained by the procedure described in Sec. 4.3. The results are too optimistic, as correlations are neglected.

	energy scale	energy scale normalised	energy scale $\cos\theta_z$-dependent	energy scale $\cos\theta_z$-dependent not normalised	
current uncertainty	10	10	10	10	
$1\,\sigma$	-0.6 $+0.4$	-10.7 $+22.6$	-2.0 $+1.6$	-1.2 $+0.9$	
$3\,\sigma$	-1.8 $+1.4$	-26.8 $+74.1$	-5.6 $+5.0$	-3.0 $+2.6$	
	flux normalization	zenith $(\cos\theta_z)$ slope	$\frac{\nu_\mu+\overline{\nu}_\mu}{\nu_e+\overline{\nu}_e}$	$\nu_\mu/\overline{\nu}_\mu$	$\nu_e/\overline{\nu}_e$
current uncertainty	15	4	2	10	10
$1\,\sigma$	-1.1 $+1.1$	-2.2 $+2.3$	-8.6 $+10.0$	-6.4 $+6.9$	-22.2 $+33.9$
$3\,\sigma$	-3.3 $+3.3$	-6.4 $+7.3$	-23.3 $+34.5$	-18.0 $+22.2$	-54.9 $+168.5$
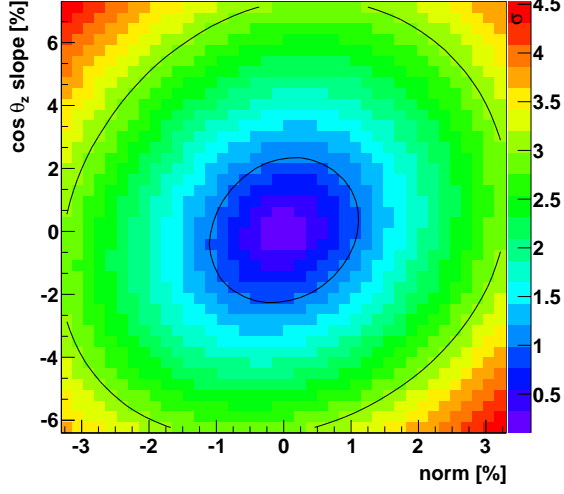
Figure C.1: Correlation of flux normalization and zenith slope - uncorrelated by definition.
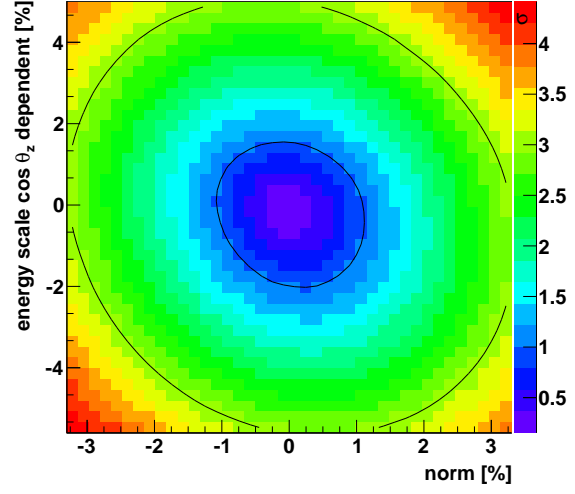
Figure C.2: Correlation of flux normalization and $\cos\theta_z$-dependent energy scale - uncorrelated by definition.
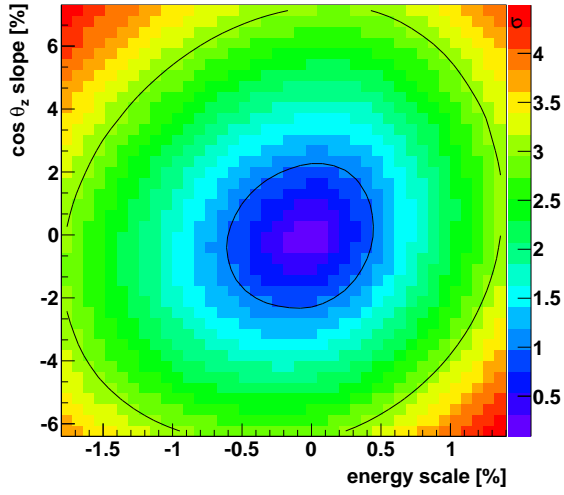
Figure C.3: Correlation of energy scale and zenith slope - uncorrelated by definition.
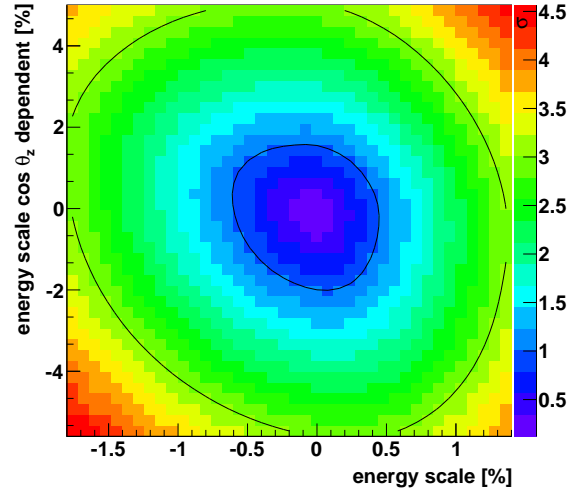
Figure C.4: Correlation of energy scale and $\cos\theta_z$-dependent energy scale - uncorrelated by definition.
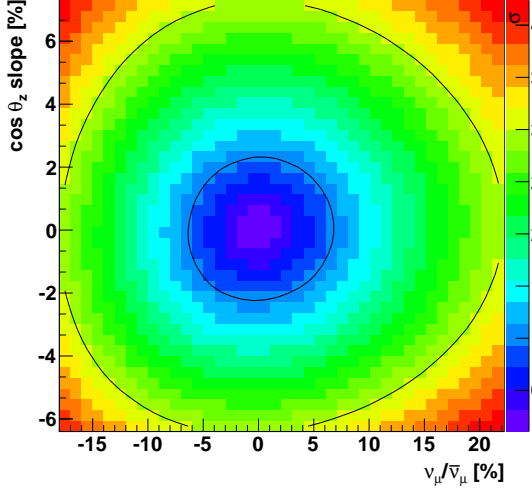
Figure C.5: Correlation of $\nu_\mu/\overline{\nu}_\mu$ ratio and zenith slope - uncorrelated.
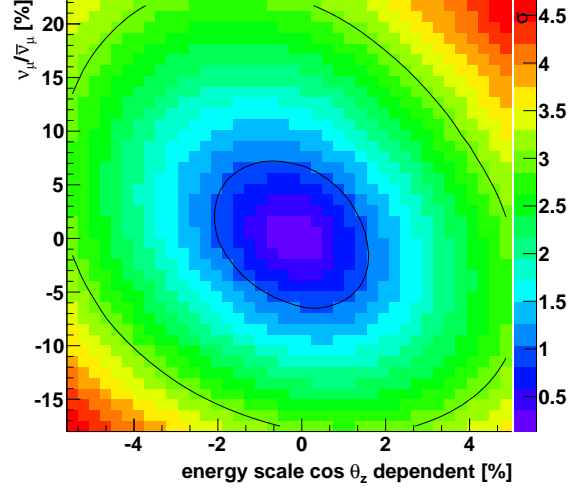
Figure C.6: Correlation $\nu_\mu/\overline{\nu}_\mu$ ratio and $\cos\theta_z$-dependent energy scale - uncorrelated.
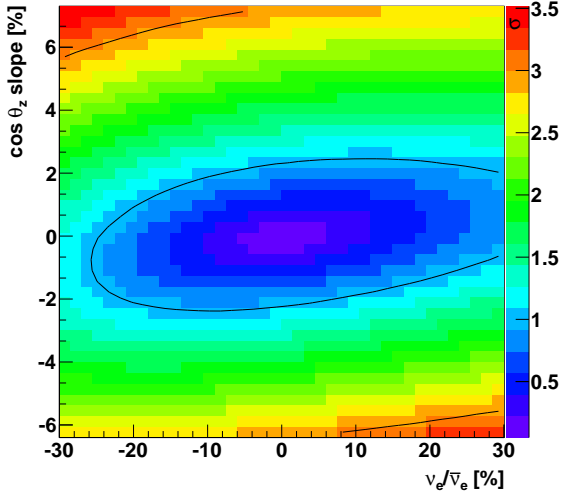
Figure C.7: Correlation $\nu_e/\overline{\nu}_e$ ratio and zenith slope - weakly correlated, but the uncertainty on the ratio is much higher.
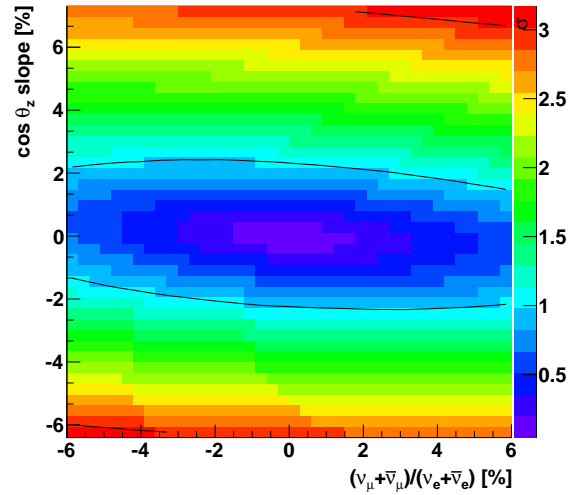
Figure C.8: Correlation $(\nu_\mu + \overline{\nu}_\mu)/(\nu_e + \overline{\nu}_e)$ ratio and zenith slope - weakly correlated, but the uncertainty on the ratio is much higher.
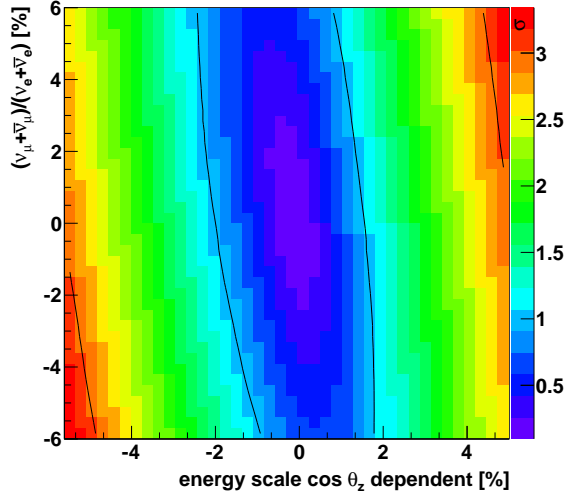
Figure C.9: Correlation of $\cos\theta_z$-dependent energy scale and $(\nu_\mu + \overline{\nu}_\mu)/(\nu_e + \overline{\nu}_e)$ ratio - weakly correlated, but the uncertainty on the ratio is much higher.
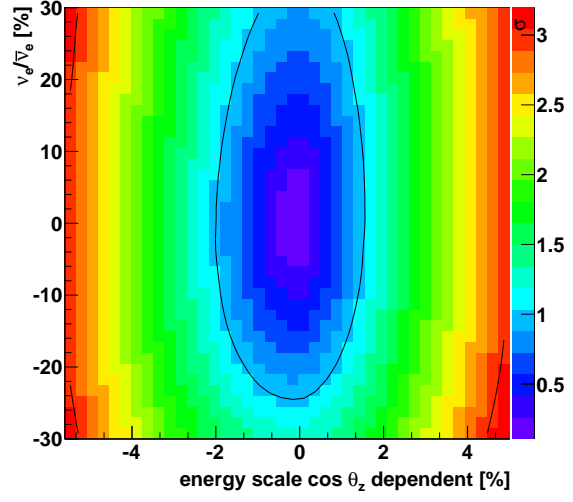
Figure C.10: Correlation of $\cos\theta_z$-dependent energy scale and $\nu_e/\overline{\nu}_e$ ratio - weakly correlated, but the uncertainty on the ratio is much higher.
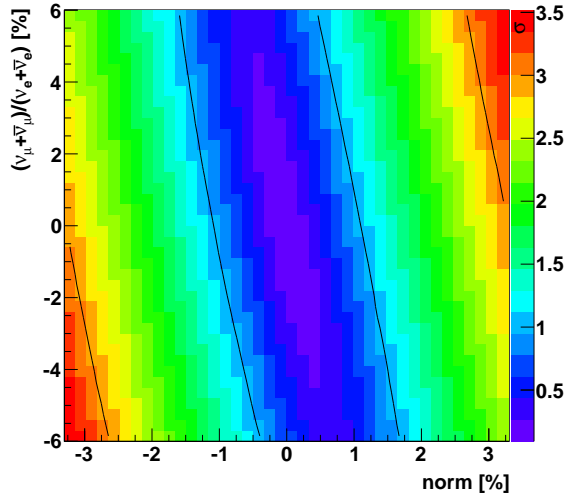
Figure C.11: Correlation of flux normalization and $(\nu_\mu + \overline{\nu}_\mu)/(\nu_e + \overline{\nu}_e)$ ratio - weakly correlated due to cross-sections.
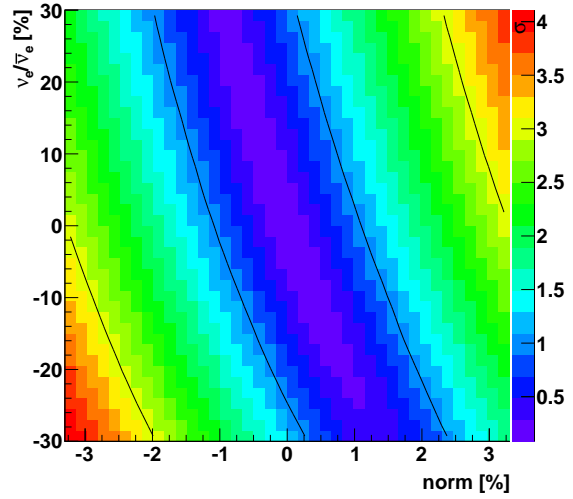
Figure C.12: Correlation of flux normalization and $\nu_e/\overline{\nu}_e$ ratio - weakly correlated due to cross-sections.
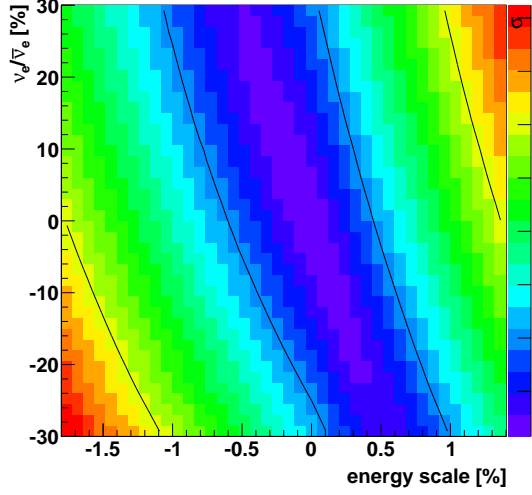
Figure C.13: Correlation of energy scale and $\nu_e/\overline{\nu}_e$ ratio - weakly correlated due to cross-sections.
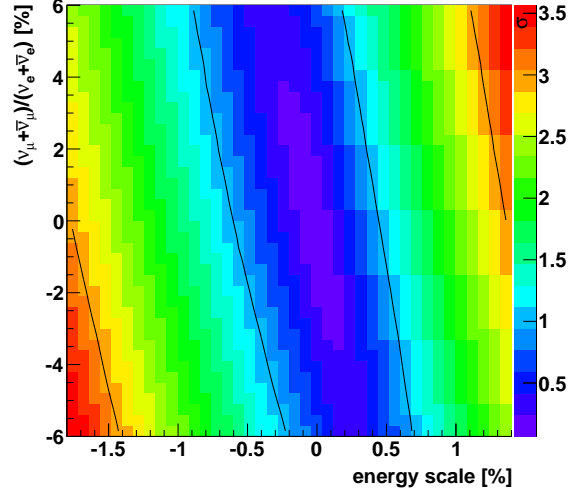
Figure C.14: Correlation of energy scale and $(\nu_\mu + \overline{\nu}_\mu)/(\nu_e + \overline{\nu}_e)$ ratio - weakly correlated due to cross-sections.
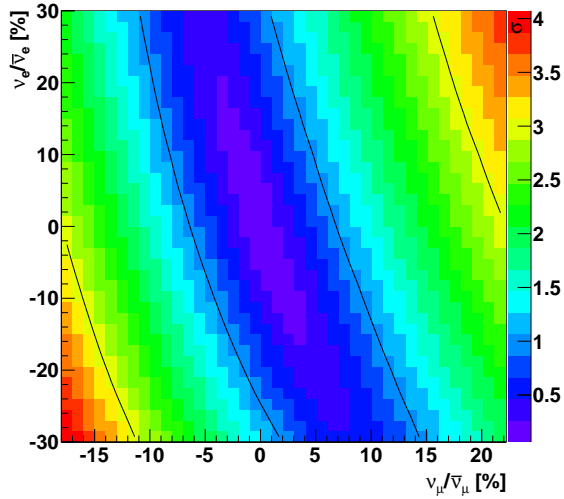
Figure C.15: Correlation of $\nu_\mu/\overline{\nu}_\mu$ and $\nu_e/\overline{\nu}_e$ ratio - weakly correlated due to cross-sections.
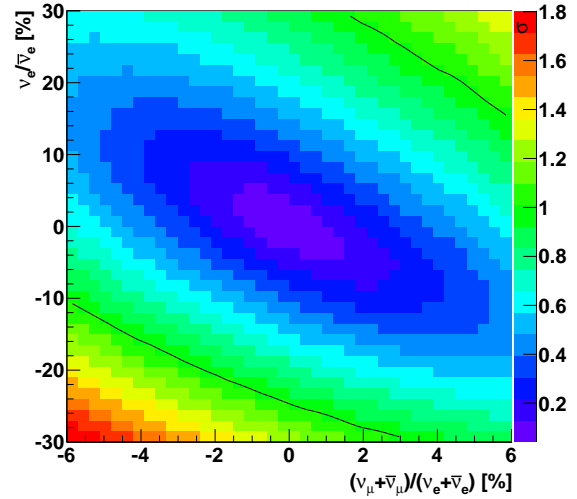
Figure C.16: Correlation of $(\nu_\mu + \overline{\nu}_\mu)/(\nu_e + \overline{\nu}_e)$ and $\nu_e/\overline{\nu}_e$ ratio - weakly correlated.

List of Figures

List of Tables

Bibliography

[1] R. Davis, D. S. Harmer, and K. C. Hoffman, *Search for neutrinos from the sun.*, *Phys.Rev.Lett.* **20** 1205–1209 (1968).

[2] *http://upload.wikimedia.org/wikipedia/commons/3/3a/Cosmicrayshower.png*.

[3] C. Patrignani et al. (Particle Data Group), *The Review of Particle Physics*, *Chin. Phys. C* **40** 100001 (2016).

[4] S. Cecchini and M. Spurio, *Atmospheric muons: experimental aspects*, (2012), [`arXiv:1208.1171`].

[5] M. Bazzotti, S. Biagi, G. Carminati, S. Cecchini, and T. Chiarusi, *Atmospheric MUons from PArametric formulas: a fast GEnerator for neutrino telescopes (MUPAGE)*, (2009), [`arXiv:0907.5563`].

[6] Carlo Giunti and Chung W. Kim., *Fundamentals of Neutrino Physics and Astrophysics*, (2007).

[7] L. Wolfenstein, *Neutrino oscillations in matter.*, *Phys. Rev. D* **17** 2369 (1978).

[8] Q. R. Ahmad et al., *Direct Evidence for Neutrino Flavor Transformation from Neutral-Current Interactions in the Sudbury Neutrino Observatory*, *Phys. Rev. Lett.* **89** 011301 (2002), [`nucl-ex/0204008`].

[9] E. K. Akhmedov, *Parametric resonance in neutrino oscillations in matter*, *Pramana* **54** 47–63 (2000), [`hep-ph/9907435`].

[10] A. de Gouvea et al., *Intensity Frontier Neutrino Working Group, Working group report: Neutrinos*, (2013), [`arXiv:1310.4340`]. Community Summer Study 2013: Snowmass on the Mississippi (CSS2013) Minneapolis, MN, USA.

[11] F. P. An et al., *Observation of electron-antineutrino disappearance at Daya Bay*, *Phys. Rev. Lett.* **108** 171803 (2012), [`arXiv:1203.1669`].

[12] E. K. Akhmedov, S. Razzaque, and A. Y. Smirnov, *Mass hierarchy, 2-3 mixing and CP-phase with Huge Atmospheric Neutrino Detectors*, *JHEP* **02** 082 (2013), [`arXiv:1205.7071`].

[13] KM3NeT Collaboration, S. Adrián-Martínez et al., *Letter of Intent for KM3NeT 2.0*, *J. Phys. G: Nucl. Part. Phys.* **43** 084001 (2016), [`arXiv:1601.7459`].

[14] J. Brunner, *Updated tag list for the new ANTARES event format. ANTARES internal note (ANTARES-Soft/1999-003)*, (1999).

[15] C. Andreopoulos et al., *The GENIE Neutrino Monte Carlo Generator.*, *Nucl. Instrum. Meth. A* **614** 87–104 (2010), [`arXiv:0905.2517`].

[16] G. D. Barr, T. K. Gaisser, P. Lipari, S. Robbins, and T. Stanev, *A three-dimensional calculation of atmospheric neutrinos*, *Phys.Rev. D* **70** 023006 (2004), [`astro-ph/0403630`].

[17] C. Kopper, *A software framework for KM3NeT.*, *Nucl. Instrum. Meth. A* **602** 107 (2009).

[18] IceCube Collaboration, O. Schulz and M. Spurio, *Implementation of an active veto against atmospheric muons in IceCube DeepCore*, *Proceedings of the 31th International Cosmic Ray Conference (ICRC)* (2009).

[19] E. Richard, K. Okumura, K. Abe, et al., *Measurements of the atmospheric neutrino flux by Super-Kamiokande: energy spectra, geomagnetic effects, and solar modulation*, *Phys. Rev. D* **94** 052001 (2016), [`arXiv:1510.08127`].

[20] CNRS/CC-IN2P3, *Centre de Calcul IN2P3/CNRS*, . Website. Available online at *http://cc.in2p3.fr.*

[21] J. Hofestädt, *Measuring the neutrino mass hierarchy with the future KM3NeT/ORCA detector.* doctoral thesis, Univ. Erlangen-Nürnberg, 2016.

[22] S. Wagner, *Search for cosmic neutrino emission from Milagro sources with ANTARES*, doctoral thesis, Univ. Erlangen-Nürnberg, 2015.

[23] T. K. Gaisser and M. Honda, *Flux of Atmospheric Neutrinos*, *Ann.Rev.Nucl.Part.Sci.* **52** 153–199 (2002), [`hep-ph/0203272`].

[24] G. Battistoni, A. Ferrari, T. Montaruli, and P. R. Sala, *The FLUKA atmospheric neutrino flux calculation*, *Astropart.Phys.* **19** 269–290 (2002), [`hep-ph/0207035`].

[25] M. Honda, M. Sajjad Athar, T. Kajita, K. Kasahara, and S. Midorikawa, *Atmospheric neutrino flux calculation using the NRLMSISE00 atmospheric model*, *Phys. Rev. D* **92** 023004 (2015), [`arXiv:1502.3916`]. `http://www.icrr.u-tokyo.ac.jp/~mhonda/`.

[26] T. Sanuki, M. Honda, T. Kajita, K. Kasahara, and S. Midorikawa, *Study of cosmic ray interaction model based on atmospheric muons for the neutrino flux calculation*, *Phys. Rev. D* **75** 043005 (2007), [`astro-ph/0611201`].

[27] M. Honda, T. Kajita, K. Kasahara, S. Midorikawa, and T. Sanuki, *Calculation of atmospheric neutrino flux using the interaction model calibrated with atmospheric muon data*, *Phys. Rev. D* **75** 043006 (2007), [`astro-ph/0611418`].

[28] M. Honda, T. Kajita, K. Kasahara, and S. Midorikawa, *Improvement of low energy atmospheric neutrino flux calculation using the JAM nuclear interaction model*, *Phys. Rev. D* **83** 123001 (2011), [`arXiv:1102.2688`].

[29] T. Kajita, *Observation of atmospheric neutrinos*, *REVIEWS OF MODERN PHYSICS* **73** (2001).

[30] T. Kajita, *Atmospheric Neutrinos*, *Advances in High Energy Physics* **2012** 504715 (2012).

[31] T. Kajita, *The Measurement of Neutrino Properties with Atmospheric Neutrinos*, *Annu. Rev. Nucl. Part. Sci.* **64** 343–362 (2014).

[32] P. Lipari, *The fluxes of sub–cutoff particles detected by AMS, the cosmic ray albedo and atmospheric neutrinos*, *Astropart.Phys.* **16** 295–323 (2001), [`astro-ph/0101559`].

[33] Y. Ashie, J. Hosaka, K. Ishihara, Y. Itow, et al., *A Measurement of Atmospheric Neutrino Oscillation Parameters by Super-Kamiokande I*, *Phys.Rev. D* **71** 112005 (2005), [`hep-ex/0501064`].

[34] G. D. Barr, S. Robbins, T. K. Gaisser, and T. Stanev, *Uncertainties in Atmospheric Neutrino Fluxes*, *Phys.Rev. D* **74** 094009 (2006), [`astro-ph/0611266`].

[35] J. Evans, D. G. Gamez, et al., *Uncertainties in Atmospheric Muon-Neutrino Fluxes Arising from Cosmic-Ray Primaries*, (2016), [arXiv:1612.03219].

[36] J. A. Formaggio and G. P. Zeller, *From eV to EeV: Neutrino Cross-Sections Across Energy Scales*, *Rev. Mod. Phys.* **84** 1307 (2013), [arXiv:1305.7513].

[37] S. Hallmann, *Sensitivity of ORCA to the neutrino mass hierarchy*, bachelor thesis, Univ. Erlangen-Nürnberg, 2013.

[38] J. Brunner, *Counting Electrons to Probe the Neutrino Mass Hierarchy*, (2013), [arXiv:1304.6230].

[39] KM3NeT Collaboration, S. Adrián-Martínez et al., *Intrinsic limits on resolution of muon and electron charged-current neutrino events in KM3NeT/ORCA-style detectors*, (2016), [arXiv:1612.05621].

Acknowledgements

In the end I want to thank some important people without whom this work wouldn't have been possible.

First my great thanks go to Dr. Thomas Eberl, who supervised my work in a very kind way. Then special thanks go to Dr. Jannik Hofestädt, who introduced me into all the methods I used and kindly replied to every question which arose during this work.

Finally I give my thanks to my parents Claudia and Manfred Volkert, who supported me in all possible ways that are open for non-physicists.

Erklärung

Hiermit erkläre ich, diese Masterarbeit in Eigenarbeit angefertigt zu haben, sofern nicht explizit in Text oder Referenzen vermerkt. Diese Arbeit ist der Universität Erlangen-Nürnberg als Vorraussetzung für den Erhalt des Abschlusses Master of Science vorgelegt worden. Ich erkläre, dass diese Arbeit weder partiell noch als Ganzes für den Erhalt eines anderweitigen Abschlusses verwendet wurde und wird.

Erlangen, 03.02.2017
_____
Ort, Datum

_____
Marco Volkert